DISSERTATION

COHERENT RAMAN SPECTROSCOPY FOR SUPERSONIC FLOW MEASUREMENTS

Submitted by

Gregory C. Herring

Physics Department

In partial fulfillment of the requirements

for the Degree of Doctor of Philosophy

Colorado State University

Fort Collins, Colorado

Fall 1987

COLORADO STATE UNIVERSITY

AUGUST 1987

WE HEREBY RECOMMEND THAT THE THESIS PREPARED UNDER OUR SUPERVISION BY GREGORY C. HERRING ENTITLED "COHERENT RAMAN SPECTROSCOPY FOR SUPERSONIC FLOW MEASUREMENTS" BE ACCEPTED AS FULFILLING IN PART REQUIREMENTS FOR THE DEGREE OF DOCTOR OF PHILOSOPHY.

Committee on Graduate Work

William M. Fairbank Jr.

Sie An Lee

Lawrence N. Hadley

C. Gian-yan Su

Advisor

Robert K. Seisure

Department Head

ABSTRACT OF DISSERTATION

COHERENT RAMAN SPECTROSCOPY FOR
SUPERSONIC FLOW MEASUREMENTS

Inverse Raman spectroscopy is used to measure non-intrusively the velocity, temperature, and density in a supersonic nitrogen gas flow. The present measurement uses two lasers, operating at different visible frequencies, to drive coherently the vibrational resonances in the flowing N_2. A miniature wind tunnel produces the Mach 2 supersonic flow. Flow velocities are determined by measuring the flow induced Doppler shift of the Q-branch vibrational Raman transitions, while the rotational temperature is deduced from the relative strengths of two adjacent rotational lines in the Q-branch. Densities are obtained using the temperature measurement along with a measurement of the relative strength of a single rotational transition between the unknown flow density and a known reference density. Statistical measurement uncertainties are approximately 3% for velocities, 3% for temperatures, and 10% for densities. The measurements are in general agreement with the approximations of a one-dimensional supersonic flow model.

In addition to flow parameter measurements, the properties of the coherent Raman process are also studied. Signal-to-noise ratios for two different coherent Raman processes (inverse Raman scattering and coherent Stokes Raman scattering) are about the same for the conditions in this experiment. The absolute signal strengths of both

of these coherent Raman processes are found to be in rough agreement with those expected from theory. Finally, pressure broadening coefficients for three Q-branch rotational transitions (J = 8, 9, 10) in the $v = 0 \rightarrow 1$ vibrational transition in N_2 are measured and are in good agreement with other measurements recently reported.

Gregory C. Herring
Department of Physics
Colorado State University
Fort Collins, CO 80523
Fall, 1987

ACKNOWLEDGMENTS

First, I would like to thank Prof. Chiao-Yao She for the guidance and time that he has provided throughout this project. Secondly, I would like to thank Profs. William M. Fairbank, Jr. and Siu Au Lee for the time that they have devoted to this project. I also thank each of the above mentioned for their contributions to other experiments that I have worked on as a graduate student and for their contribution to my development as a research scientist. I am also grateful to Louis Hlousek and John Prodan for their help in the initial stages of my laboratory work at CSU. I would also like to thank Prof. Lawrence Hadley for his critical reading of this manuscript. Hans Moosmüller helped with the final stages of these measurements. Prof. Virgil Sandborn and Prof. Willy Sadeh have participated in many helpful discussions on supersonic flow. Finally, I thank Faye Knowles for typing this manuscript.

TABLE OF CONTENTS

LIST OF TABLES

LIST OF FIGURES

CHAPTER 1

Introduction

Supersonic flow velocities have traditionally been measured using macroscopic probes (i.e., pitot tubes, hot-wire anemometers) which physically disturb the flow itself. Thus aerodynamicists have long been interested in less intrusive methods for measuring flow velocities. Over the last 20 years, lasers have been introduced as tools for noninvasive flow measurements. Early work[1,2] utilized Mie scattering off of seeded and naturally occurring particles in subsonic flows. This technique is inadequate at supersonic velocities because the Mie scatterers are no longer able to accurately follow the flow. More recently, new techniques have been demonstrated which employ light scattering off atoms or molecules, which are able to follow the high speed flows. The subject of this thesis is one of these new techniques: coherent Raman scattering.

The main achievement of this work is a laboratory demonstration[3] of supersonic velocity measurements in N_2 using inverse Raman spectroscopy. This technique is one of several coherent Raman techniques that uses two lasers operating at different optical frequencies. Vibrational transitions in the N_2 molecule are induced when the frequency difference of the two lasers matches a vibrational transition frequency. Velocities were determined by measuring the first order Doppler shift of a single Q-branch vibrational transition. The

Doppler shift is measured by comparing the transition frequency for a high speed flow with the transition frequency for a stationary sample. The flow velocity is obtained from the frequency shift since the velocity and shift are proportional to one another. Before the present use of inverse Raman spectroscopy, stimulated Raman gain spectroscopy was used to demonstrate a subsonic flow velocity measurement.[4] Simultaneous with this early work, Gustafson et al. have used coherent anti-Stokes Raman spectrosocpy for a velocity measurement[5] in CH_4.

One advantage of the coherent Raman method is that it can also measure the temperature and density of the flow. In the present work, the same inverse Raman technique was also used to demonstrate rotational temperature and density measurements in the supersonic flow. Rotational temperatures were obtained by measuring the relative strengths of two or more Q-branch vibrational transitions. The temperatures were determined by comparing the relative strengths of two adjacent rotational transitions to a Boltzman distribution. Density measurements were made by comparing the transition strength of a single transition for both the unknown supersonic flow density and a known reference density. The relative transition strength was obtained by measuring the relative area under the line for both densities. Since the gas density is proportional to the transition strength, the unknown flow density was determined from the product of the known reference density and the ratio of the measured relative areas.

In addition to non-intrusive velocity, temperature and density measurements, there are other strong advantages to the use of

coherent Raman spectroscopy for flow parameter measurements. There is no seeding required since the measurements are made directly on the N_2 (or any other molecular) flow medium. Crossing the beams of the two lasers provides spatial resolution of 1 mm and the capability of simultaneously measuring all three perpendicular velocity components. Recently, the possibility of complete velocity measurements in a single 10 nsec laser pulse has been proposed.[6] Thus coherent Raman methods have the potential of becoming powerful tools for probing supersonic flows.

In principle, the simpler technique of spontaneous Raman scattering could also be used to measure flow velocities. However, a major disadvantage of the spontaneous technique is that the signal depends linearly on the laser power. Using commonly available lasers, the spontaneous technique generally produces about 10^6 times less signal than a comparable inverse Raman technique, which has a signal that depends on the product of the laser powers. Thus the spontaneous method would require far more time to make a measurement with the same accuracy as that obtained using a coherent method. Typically one might want to make measurements on 10^{18} cm^{-3} molecules of N_2 with 10 nsec, 1.0 MW laser pulses. Under these conditions, the spontaneous Raman technique would have a signal strength on the order of 1 photon per 10 laser pulses for a 1.0 meter spectrometer (f/6) with a 5 μm slits (10 GHz resolution). On the other hand, an inverse Raman experiment (using a 10 mW cw probe laser with the 1.0 MW pulsed laser) would produce 10^6 signal photons per pulse. Although this large signal is on top of the noisy probe-laser background, the

signal-to-noise ratio would still be much better than the spontaneous Raman signal-to-noise ratio.

A second disadvantage of the spontaneous technique is the low spectral resolution, which would be limited to 10 GHz for the spectrometer described above. In contrast, the spectral resolution of the inverse Raman spectrometer is limited by the laser linewidths and would typically be 100 MHz. Since the Doppler shifts expected for Mach 1.0 flow are 0.1 GHz (forward scattering) to 1.0 GHz (backward scattering) the higher resolution inverse Raman technique has a clear advantage over the lower resolution spontaneous technique.

Other light scattering techniques for non-intrusive velocity measurements have both advantages and drawbacks when compared to coherent Raman spectroscopy. The first, acousto-optic light scattering,[7] has the advantage of an uncomplicated apparatus compared to the coherent Raman method. In addition, acousto-optic uncertainties for velocity and temperature measurements are presently smaller than those for coherent Raman techniques. However, acousto-optic velocimeters rely on acoustic disturbances propagating both upstream and downstream in the flow. But an upstream propagation is impossible for a supersonic flow. Thus, the acousto-optic technique is unsuitable for measuring supersonic velocities.

A second competitor is laser induced fluorescence, which also has a less complicated experimental arrangement than coherent Raman spectroscopy. Fluorescence techniques[8,9,10] require seeding the flow medium with a small concentration of either Na or I_2, monitoring the fluorescence, and measuring either the flow-induced Doppler shift or the transit time through the laser beams. Current schemes have the

ability to measure as many as 10,000 spatial points simultaneously. The prospects for simultaneous multipoint measurements using coherent Raman spectroscopy are discussed in the conclusion. Regardless of the above arguments, there are situations where Na or I_2 seeding is not desirable and these situations are ideal candidates for the coherent Raman technique.

All coherent Raman and fluorescence based velocity measurements to date have been made at pressures of 0.1 atm or less. At pressures of one to ten atmospheres, both of these techniques suffer losses in accuracy because of pressure broadening of their respective spectral lines. In contrast to Raman and fluorescence spectral lines, Rayleigh-Brillouin spectral lines become narrower with increasing pressure, making a Rayleigh-Brillouin technique more suitable for velocity measurements at high pressures. A velocity measurement at 1 atm using stimulated Rayleigh-Brillouin spectroscopy has already been demonstrated.[11] Since the Rayleigh-Brillouin and Raman experimental apparatuses are similar, the two techniques would complement each other in a single system capable of both low and high pressure velocity measurements.

The following summary is an outline of the rest of this thesis. In Chapter II a classically oriented description of coherent Raman scattering is presented. A one-dimensional supersonic flow model is outlined in Chapter III. Chapter IV contains the details of the experimental apparatus used to make the flow measurements. The results of these measurements are presented in Chapter V, along with a comparison to one-dimensional inviscid and viscous flow models. Chapter V also contains the results of signal strength measurements

for two of the coherent Raman techniques and the results of pressure broadening measurements in the Q-branch of N_2. Finally, Chapter VI contains a summary and a discussion of future work for developing the coherent Raman technique into a diagnostic tool for flow measurement.

CHAPTER 2

Coherent Raman Spectroscopy

This chapter will describe the stimulated Raman effect and its associated spectroscopies. The approach shall be primarily classical in nature, using the results of quantum mechanics in situations where classical mechanics fails conceptually. The purpose of a theoretical discussion here is to provide a simple and physical understanding of stimulated Raman scattering, rather than calculating its effects from first principles. The classical theory is suitable for this purpose. In particular, it can provide a formula relating the nonlinear Raman susceptibility and the coherent Raman gain to the independently measurable differential Raman cross section.

In Section II-1 a brief overview of the induced linear and non-linear polarization of matter will be presented. Both the non-linear and linear Raman effects are described as a modulation of this induced polarization due to vibrations of the molecular nuclei. The classical electromagnetic theory will then be used to describe the Raman signal generated by this non-linear polarization. Other theoretical areas of interest to this thesis are the Doppler effect for coherent Raman processes and the energy level population distributions in diatomic molecules. These are discussed in Sections II-2 and II-3 respectively.

2.1.1 Induced Polarization of Matter

When an electromagnetic (EM) wave traverses a material medium it induces a net polarization in the material. In SI units, the induced polarization is described in terms of the electric susceptability per molecule, χ, as

$$P = \epsilon_o N\chi E \qquad 2.1$$

where ϵ_o is the vacuum permittivity, N is the number of molecules per unit volume, $\epsilon_o \chi$ is the polarizability and E is the applied electric field. For small fields, χ is independent of the field strength. For large electric fields, χ is no longer independent of the electric field[12] and P is no longer dependent linearly on the electric field. If χ is expanded as

$$\chi = \chi_1 + \chi_2 E + \chi_3 E^2 + \ldots, \qquad 2.2$$

the polarization in Eq. (1) becomes

$$P = \epsilon_o N (\chi_1 E + \chi_2 E^2 + \chi_3 E^3 + \ldots), \qquad 2.3$$

where χ_1, χ_2, etc., are the first, second, etc., order susceptabilities in electric field strength. Although Eq. (2.3) is written as a scalar relation, in general P and E are vectors, while χ_1, χ_2, etc., are second, third, etc. rank tensors, respectively. In solids, for example, the applied field, E, and the induced polarization, P, may not point in the same direction. However, the present analysis

will be applied to situations (isotropic medium) with linearly polarized electric fields with all fields and polarizations in the same direction. Thus, the vector and tensor nature of the quantities in Eq. (2.3) can be ignored, and the above scalar relations will be sufficient for this treatment.

The quantities χ_1, χ_2, etc. can be used to describe a number of well known scattering phenomena. The first term (linear polarization) is responsible for the refractive index and spontaneous Rayleigh scattering. The non-linear χ_2 term describes second-harmonic generation while the χ_3 term gives rise to third-harmonic generation, etc. For homogeneous and isotropic media, χ_2 is zero.[13] Throughout this analysis only diatomic gases are considered and thus the χ_3 terms are the lowest order non-linear effects to be expected.

Rotational and vibrational motion of the molecule can modulate the polarization that is induced due to applied electric field. For example, consider a vibrating diatomic molecule with an induced polarization from an externally applied field. The magnitude of this induced polarization will be altered as the internuclear distance changes. The electric field and molecular vibrational frequencies will mix together to produce polarization components at frequencies shifted from the original applied field frequency. This polarization (in this case vibrational) and accompanying radiation is known as the Raman effect. The vibrationally dependent polarization can be described in the first approximation as being proportional to the coordinate characterizing the vibrational motion, q. Mathematically,

the susceptibility, χ, is expanded as a Taylor series where the second and higher order terms in q are neglected. Then

$$\chi = \chi_o + \left(\frac{\partial \chi}{\partial q}\right)_o q \ , \qquad 2.4$$

where the susceptibility χ_o represents the vibration independent Rayleigh polarization, $(\partial\chi/\partial q)q$ represents the susceptibility for the vibrational Raman polarization, and q is the coordinate describing the vibration. In general, there will be additional terms in Eq. (2.4) due to higher-order vibrational motions or other types of non-electronic motions in the medium. In this work, only first order vibrational motion shall be considered. The form of the polarization generated by the Raman effect between vibrational levels is

$$P = \epsilon_o N \left(\frac{\partial \chi}{\partial q}\right)_o qE \quad . \qquad 2.5$$

In Eq. (2.5), the anharmonicity in molecular vibration has been ignored; the vibration amplitude q may, however, depend on the applied electric fields. For small fields, q is independent of electric field and Eq. (2.5) describes the source for spontaneous Raman scattering. Under strong applied fields, q may be driven coherently by the beating of two fields in resonance with the molecular vibration. This field-dependent q gives rise to a third-order nonlinear susceptibility and is responsible for stimulated or coherent Raman scattering.

Once the polarization due to the external field is known, one can calculate any additional fields generated by the induced

polarization by using Maxwell's equations. As these newly generated fields gain energy, the original incident field energy must be reduced. This in turn reduces the induced polarization which, in turn, reduces the magnitude of the radiated fields. In general, the two expressions describing the interplay between the incident and the newly radiated fields via the induced polarization must be solved self consistently to obtain a correct solution. If the newly generated fields are small compared to the incident field, the incident field energy can be approximated as constant and the energy depletion ignored. In this treatment, the depletion of the applied fields is assumed to be negligible. Section 2.1.2 shall derive the form of the non-linear polarization for a vibrational Raman transition, while Section 2.1.3 will derive the radiated electric fields from electromagnetic theory.

2.1.2 Non-Linear Vibrational Raman Polarization

The purpose of this section is to calculate the time (or frequency) dependence of the non-linear Raman polarization. The procedure is to first find how the external force, which is exerted on the vibrating molecule, depends on the incident electric field. Next the vibrating molecule is modeled as a driven harmonic oscillator, and the effective displacement is derived. This field dependent displacement and Eq. (2.5) then yield the third order Raman polarization. Finally, the expression is related to differential cross section, $d\sigma/d\Omega$ which is the commonly measured experimental parameter.

Consider a molecule (without a permanent dipole moment) with only an induced dipole moment $\epsilon_o \chi E$. The interaction energy for an applied field E is

$$W = \frac{\epsilon_o}{2} \chi E^2 \quad . \tag{2.6}$$

For the Raman process, the factor χ is replaced with $(\partial\chi/\partial q)q$. The force associated with this interaction energy is

$$F = \frac{\partial W}{\partial q} = \frac{\epsilon_o}{2} \frac{\partial \chi}{\partial q} E^2 \quad . \tag{2.7}$$

Now consider a medium that is subjected to two independent electric fields at frequencies ω_1 and ω_2, where $\omega_2 > \omega_1$ and

$$E_1 = \frac{1}{2} \left[E_{01} e^{-i\omega_1 t} + c.c.\right] \tag{2.8a}$$

$$E_2 = \frac{1}{2} \left[E_{02} e^{-i\omega_2 t} + c.c.\right] \tag{2.8b}$$

Here $i = \sqrt{-1}$, c.c. stands for complex conjugate terms, and the spatial dependence is contained in the factors E_{01} and E_{02}. Substituting the quantity $E_1 + E_2$ for E and keeping only terms at frequency $\omega_2 - \omega_1$, Eq. (2.7) becomes

$$F = \frac{\epsilon_o}{4} \frac{\partial \chi}{\partial q} \left[E_{01}^* E_{02} e^{-i(\omega_2 - \omega_1)t} + c.c.\right] \quad . \tag{2.9}$$

The neglected terms are all at zero frequency (corresponding to an average dc polarization or frequencies $(2\omega_1, 2\omega_2, \omega_1 + \omega_2)$ too large

to couple to the relatively slower vibrational motion of the molecule.

The vibrating molecule is now modeled as a driven, damped harmonic oscillator with natural vibration frequency Δ. The external driving force is given by Eq. (2.9). The damping force, $\gamma(\partial q/\partial t)$, accounts for spontaneous relaxation. The equation of motion becomes

$$\frac{\partial^2 q}{\partial t^2} + \gamma \frac{\partial q}{\partial t} + \Delta^2 q = F \quad , \tag{2.10}$$

where the mass of the oscillator was taken to be unity. Substituting in the solution

$$q(t) = \frac{1}{2}\left[q_o\, e^{-i\omega t} + c.c.\right] \tag{2.11}$$

where $\omega = \omega_2 - \omega_1$, the expression for q_o, with $\omega + \Delta \approx 2\Delta$, becomes

$$q_o = \frac{\epsilon_o}{4\Delta} \frac{\partial \chi}{\partial q}\left\{\frac{E_{01}^{*}\, E_{02}}{(\Delta-\omega) - \frac{i\gamma}{2}}\right\} \quad . \tag{2.12}$$

This solution can be substituted into Eq. (2.5) to determine the frequency dependence of the non-linear polarization.

The medium is being irradiated by two independent electric fields at frequencies ω_1 and ω_2. Thus Eq. (2.5) gives rise to four separate polarizations terms. Substituting the expression $E = E_1 + E_2$ and the solution for q(t) into Eq. (2.5) gives the result

$$P(t) = \frac{N\epsilon_o}{4} \frac{\partial \chi}{\partial q}\left[q_o^{*} E_{01} e^{-i(2\omega_1-\omega_2)t} + q_o E_{01} e^{-i\omega_2 t} + q_o E_{02} e^{-i(2\omega_2-\omega_1)t} + q_o^{*} E_{02} e^{-\omega_1 t} + c.c.\right] \tag{2.13}$$

It can be seen that this polarization oscillates at four separate frequencies, ω_1, ω_2 and $2\omega_1 - \omega_2 \equiv \omega_3$ and $2\omega_2 - \omega_1 \equiv \omega_4$. If this polarization is also written in the form

$$P(t) = \frac{1}{2}\left[\sum_j P(\omega_j) e^{-i\omega_j t} + c.c.\right] \qquad 2.14$$

and compared with Eq. (2.13), the time independent magnitudes, $P(\omega_j)$, can be written as:

$$P(\omega_1) = \frac{1}{2} N \epsilon_o \frac{\partial \chi}{\partial q} q_o^* E_{02} \qquad 2.15a$$

$$P(\omega_2) = \frac{1}{2} N \epsilon_o \frac{\partial \chi}{\partial q} q_o E_{01} \qquad 2.15b$$

$$P(\omega_3) = \frac{1}{2} N \epsilon_o \frac{\partial \chi}{\partial q} q_o^* E_{01} \qquad 2.15c$$

$$P(\omega_4) = \frac{1}{2} N \epsilon_o \frac{\partial \chi}{\partial q} q_o E_{02} \quad . \qquad 2.15d$$

Using the expression for q_o in Eq. (2.12), the expressions for the non-linear polarizations in Eq. (2.15) become

$$P(\omega_1) = \frac{N\epsilon_o^2}{8\Delta} \left(\frac{\partial \chi}{\partial q}\right)^2 \left\{\frac{|E_{02}|^2 E_{01}}{(\Delta - \omega) + \frac{i\gamma}{2}}\right\} \qquad 2.16a$$

$$P(\omega_2) = \frac{N\epsilon_o^2}{8\Delta} \left(\frac{\partial \chi}{\partial q}\right)^2 \left\{\frac{|E_{01}|^2 E_{02}}{(\Delta - \omega) - \frac{i\gamma}{2}}\right\} \qquad 2.16b$$

$$P(\omega_3) = \frac{N\epsilon_o^2}{8\Delta} \left(\frac{\partial \chi}{\partial q}\right)^2 \left\{\frac{E_{01}^2 E_{02}^*}{(\Delta - \omega) + \frac{i\gamma}{2}}\right\} \qquad 2.16c$$

$$P(\omega_4) = \frac{N\epsilon_o^2}{8\Delta}\left(\frac{\partial\chi}{\partial q}\right)^2\left\{\frac{E_{02}^2\, E_{01}^*}{(\Delta - \omega) - \frac{i\gamma}{2}}\right\} \qquad 2.16d$$

The above expressions contain the factor, $\partial\chi/\partial q$, of which nothing is known yet. One can gain some physical feeling for $\partial\chi/\partial q$ by relating it to an easily understandable quantity, the differential scattering cross section for spontaneous Raman scattering. Consider a small scattering center irradiated by an incident field. The differential scattering cross section, $d\sigma/d\Omega$, is defined as the power radiated into a unit solid angle, in a given direction, divided by the incident intensity. This is written as

$$\frac{d\sigma}{d\Omega} = \frac{1}{I_o}\frac{dp}{d\Omega} \qquad 2.17$$

where p denotes power, Ω is the solid angle, and I_o is the incident intensity. The convention of using lower case p for power and capital P for polarization is adopted. Now consider a single isolated oscillating dipole moment with magnitude P_o and angular frequency $\omega = k/c$. The power radiated per unit solid angle, in a direction which makes angle θ with respect to the dipole axis, is given by[14]

$$\frac{dp}{d\Omega} = \frac{ck^4P_o^2\sin^2\theta}{32\,\pi^2\epsilon_o} \qquad 2.18$$

Here, as throughout most of this discussion, the index of refraction at all wavelengths will be approximated as 1.0, since only relatively low density gases are of interest. For Raman scattering perpendicular to the dipole axis, $\sin\theta = 1$ and P_o is replaced with

$\epsilon_o(\partial\chi/\partial q)q_s E$, where q_s is the vibrational amplitude associated with the spontaneous radiation. Combining Eqs. (17) and (18) with the relation between the plane wave electric field and intensity, yields the result

$$\left(\frac{\partial\chi}{\partial q}\right)^2 = \frac{16\pi^2}{q_s^2}\left(\frac{c}{\omega_1}\right)^4 \frac{d\sigma_\perp}{d\Omega} \quad , \tag{2.19}$$

where $d\sigma_\perp/d\Omega$ is the differential cross section for spontaneous scattering at frequency ω_1, at a right angle with respect to the dipole axis.

Eq. (2.19) contains the quantity q_s^2 which requires careful interpretation in dealing with spontaneous scattering. Classically, if the oscillator is at rest, q_s^2 equals zero and there can be no spontaneous radiation. To describe spontaneous radiation, it is necessary to make use of the quantum mechanical model of a vibrating diatomic molecule. Quantum mechanically, the ground state of a harmonic oscillator has a non-zero energy and thus q_s^2 is also non-zero. The expectation value of q_s^2 for a ground state oscillator is $\hbar/2\Delta$. This zero-point fluctuation is responsible for spontaneous Raman scattering. With the interpretation, $q_s^2 = \hbar/2\Delta$, Eqs. (2.16) can be rewritten as:

$$P(\omega_1) = \frac{4N\,\epsilon_o^2\,\pi^2}{\hbar}\left(\frac{c}{\omega_1}\right)^4 \frac{d\sigma_\perp}{d\Omega}\left\{\frac{|E_{02}|^2\,E_{01}}{(\Delta - \omega) + \frac{i\gamma}{2}}\right\} \tag{2.20a}$$

$$P(\omega_2) = \frac{4\,N\,\epsilon_o^2\,\pi^2}{\hbar}\left(\frac{c}{\omega_1}\right)^4 \frac{d\sigma_\perp}{d\Omega}\left\{\frac{|E_{01}|^2\,E_{02}}{(\Delta-\omega) - \frac{i\gamma}{2}}\right\} \tag{2.20b}$$

$$P(\omega_3) = \frac{4\,N\,\epsilon_o^2\,\pi^2}{\hbar}\left(\frac{c}{\omega_1}\right)^4 \frac{d\sigma_\perp}{d\Omega}\left\{\frac{E_{01}^2\,E_{02}^*}{(\Delta-\omega) + \frac{i\gamma}{2}}\right\} \tag{2.20c}$$

$$P(\omega_4) = \frac{4\,N\,\epsilon_o^{\,2}\,\pi^2}{\hbar}\left(\frac{c}{\omega_1}\right)^4 \frac{d\sigma_\perp}{d\Omega}\left\{\frac{E_{02}^{\,2}\;E_{01}^{\,*}}{(\Delta-\omega)\;-\;\frac{i\gamma}{2}}\right\} \qquad 2.20d$$

These are the magnitudes of the four polarizations which are induced by the electric field with frequencies ω_1 and ω_2.

Note that the quantum mechanical zero point fluctation is necessary for two ideas: it accounts for the spontaneous vibrational Raman scattering and it allows the third-order non-linear polarizations (Eqs. 2.16) to be written in terms of the familiar $\frac{d\sigma_\perp}{d\Omega}$ rather than the unfamiliar $\frac{\partial\chi}{\partial q}$.

In section 2.1.3, it will be shown that the polarization $P(\omega_2)$ is responsible for a radiated field at ω_2 and is called inverse Raman scattering (IRS). The component at $\omega_3 = 2\omega_1-\omega_2$ gives a radiated field at $\omega_1 - \Delta$ and is called coherent Stokes Raman scattering (CSRS). The term at ω_1 is called stimulated Raman gain scattering (SRGS) and the term at $\omega_4 = 2\omega_2-\omega_1$ is called coherent anti-Stokes scattering (CARS). The radiated fields at ω_2 (IRS), ω_3 (CSRS), ω_1 (SRGS) and ω_4 (CARS) represent the spectrum of radiation (or polarization frequencies) generated from the third order susceptibility when two separate fields at ω_1 and ω_2 are driving the vibrational motion. In the experimental work reported here, only the IRS and CSRS signals were used; thus, the treatment of the SRGS and CARS effect shall, for the most part, be omitted from further discussion.

Continuing with the description of the IRS and CSRS polarizations at ω_2 and $2\omega_1 - \omega_2$, it is worthwhile to mention a few properties of $P(\omega_2)$ and $P(\omega_3)$ before starting the description of the electromagnetic fields they generate. The expressions in Eq. (2.20) can be rewritten in the form of Eq. (2.3) as:

$$P(\omega_2) = N\,\epsilon_o\,\chi(\omega_2)|E_{01}|^2\,E_{02} \qquad 2.21a$$

$$P(\omega_3) = N\,\epsilon_o\,\chi(\omega_3)\,E_{01}^2\,E_{02}^{2*} \qquad 2.21b$$

The quantities $\chi(\omega_2)$ and $\chi(\omega_3)$ are then:

$$\chi(\omega_2) = \frac{4\epsilon_o\pi^2}{\hbar}\left(\frac{c}{\omega_1}\right)^4 \frac{d\sigma_\perp}{d\Omega}\left[\frac{1}{(\Delta-\omega) - \frac{i\gamma}{2}}\right] \qquad 2.22a$$

$$\chi(\omega_3) = \frac{4\epsilon_o\pi^2}{\hbar}\left(\frac{c}{\omega_1}\right)^4 \frac{d\sigma_\perp}{d\Omega}\left[\frac{1}{(\Delta-\omega) - \frac{i\gamma}{2}}\right] \qquad 2.22b$$

Both the real and imaginary (denoted by one and two primes respectively) components are easily obtained. The results are:

$$\chi''(\omega_2) = -\chi''(\omega_3) = \frac{2\epsilon_o\pi^2}{\hbar}\left(\frac{c}{\omega_1}\right)^4 \frac{d\sigma_\perp}{d\Omega}\left\{\frac{\gamma}{(\Delta-\omega)^2 + (\frac{\gamma}{2})^2}\right\} \qquad 2.23a$$

$$\chi'(\omega_2) = \chi'(\omega_3) = \frac{2(\Delta-\omega)}{\gamma}\,\chi''(\omega_2) \qquad 2.23b$$

It can be seen that if one of the laser frequencies is tuned such that $\omega = \omega_2-\omega_1 = \Delta$, the real parts are zero and both these polarizations become pure imaginary numbers. For the condition $\omega = \Delta$ the frequency ω_3 is just $\omega_1-\Delta$, which is the more familiar Stokes frequency from spontaneous Raman scattering.

2.1.3 Wave Propagation in a Non-Linear Medium

In this section, the electromagnetic fields generated by the polarizations in Eq. (2.20) will be described. Two different cases will be considered: the first one with all fields described as plane waves and the second one with all fields described as focused

Gaussian beams. In the plane wave case, expressions for the intensities produced by the Raman polarizations will be derived, while in the Gaussian beam case, equations for the total power generated by each of the two non-linear polarizations will be given.

The wave equation for the electric field strength, at any one of the Raman polarization frequencies, propagating through an essentially transparent medium with non-linear polarization, P_{NL}, is given by[15]

$$\nabla \times \nabla \times E - \mu_o \epsilon_o (1 + N\chi_1) \frac{\partial^2 E}{\partial t^2} = \mu_o \frac{\partial^2 P_{NL}}{\partial t^2} \qquad 2.24$$

For a wave which is propagating along the z axis, the spatial dependence (i.e., the factors E_{01} or E_{02} in Eq. (2.9) of E) is written

$$E(r,z) = \frac{1}{2} E(r) \left[e^{ikz} + c.c\right] \qquad 2.25$$

where E(r) is the as yet unspecified radial (x-y plane) dependence. Thus, both the fields generating P_{NL} and the field generated by P_{NL} can be written in the form

$$E_G = \frac{E_G(r)}{2} \left[e^{i(k_G z - \omega_G t)} + c.c.\right] \qquad 2.26$$

and the subscript, G, shall temporarily be used for the newly generated field. The quantity P_{NL} can also be written in the form

$$P_{NL} = \frac{1}{2} \left[P_o(r)\, e^{i(k_p z - \omega_p t)} + c.c.\right] \qquad 2.27$$

where k_p and ω_p represent the wavenumber and angular frequency of the induced polarization, P_{NL}. The slowly varying wave approximation[16] can now be used to simplify Eq. (2.24). This approximation assumes that the magnitude of the field generated at ω_G does not change appreciably over a distance of a few wavelengths. This can be expressed on a quantitative basis by assuming

$$\frac{\partial^2 E}{\partial z^2} << k \frac{\partial E}{\partial z} << k^2 E \quad . \tag{2.28}$$

Substituting Eqs. (2.26) and (2.27) into Eq. (2.24) and using the approximation in Eq. (2.28), the wave Eq. (2.24) is simplified to[17]

$$e^{ik_G z} \frac{dE_G}{dz} = \frac{i\omega_G}{2}\sqrt{\frac{\mu_o}{\epsilon_o}}\ P_o\ e^{ik_p z} \quad , \tag{2.29}$$

where $P_o\ e^{ik_G z}$ now represents everything in the non-linear polarization except the time dependence. In other words, P_o is just exactly those expressions given in Eq. (2.20). The method for calculating the generated Raman fields is to substitute the appropriate P_o into Eq. (2.29) and integrate over coordinates z and r.

2.1.3(a) Plane Wave Results

Consider first the case where both the incident fields, E_2 and E_1 given in Eq. (2.8), and the generated field E_G are all plane waves propagating down the z axis. A plane wave has an amplitude which is constant over all r, so the factors $E_G(r)$ in Eq. (2.29) and E(r) in Eq. (2.25) are independent of r. For the wave generated by the polarization at ω_2, Eq. (2.21a) is substituted in Eq. (2.29). In

this case, $\omega_G = \omega_p = \omega_2$ and $k_G = k_p = k_2$. Integrating from z=0 to z=ℓ, squaring the results, and considering $\omega_2 - \omega_1 \simeq \Delta$ (i.e., $\chi'(\omega_2) = 0$), the result is

$$I_2 = I_o \exp\left[-2 N \mu_o \omega_A \chi''(\omega_2) I_1 \ell\right] \quad . \qquad 2.30$$

I_2 is the total intensity at frequency ω_2 after traversing a length ℓ through the sample, while I_0 is the intensity at frequency ω_2 that was originally incident on the sample (at z=0). I_1 is the intensity at ω_1. Note that if the exponent is small compared to unity, which is usually the case for low density gases, the exponential can be expanded and approximated by its first two terms. Then the change in intensity at ω_2 is simply proportional to the product of the two intensities I_2 and I_1.

For the wave generated by the polarization at ω_3, Eq. (2.21b) is substituted into Eq. (2.29). In this case, $\omega_G = \omega_p = \omega_3 = 2\omega_1 - \omega_2$, but note that $k_G = k_3$ is not necessarily equal to $k_p = 2k_1 - k_2$ since the index of refraction varies with wavelength. Again, integrating from z=0 to z=ℓ, squaring the result and considering only the peak value by setting $\chi'(\omega_3) = 0$, the result for the polarization at ω_3 is

$$I_3 = N^2 \mu^2 \omega_3^2 |\chi(\omega_3)|^2 I_1^2 I_2 \frac{\sin^2\left(\frac{\Delta k \cdot \ell}{2}\right)}{\left(\frac{\Delta k \cdot \ell}{2}\right)^2} \ell^2 \qquad 2.31$$

where $\Delta k = 2k_1 - k_2 - k_3$ is called the wave vector mismatch. This gives the intensity generated over length ℓ at ω_3 due to the originally incident beams I_1 at ω_1 and I_2 at ω_2. The quantity I_3 is maximized when Δk is a minimum. For low density gases (< a few

atmospheres) Δk is reasonably close to zero when the fields at ω_1 and ω_2 are propagating along the same direction. For liquids or solids, where the frequency dependence of the index of refraction is substantial, the two fields ω_1 and ω_2 will have to be crossed at a specific angle in order to minimize Δk.

2.1.3(b) Focused Gaussian Beam Results

Consider now the case where both the incident fields, E_2 and E_1 and the generated fields E_G are focused Gaussian beams with the same confocal beam parameter z_0. Thus the factors E_{01} and E_{02} are of the form[18]

$$E_{01} = E_o \frac{w_o}{w} e^{ik_1 z} e^{i\eta} e^{\frac{ir^2 k_1}{2R}} e^{-\frac{r^2}{w^2}} , \qquad 2.32$$

where

$$\eta = \tan^{-1}\left(\frac{z}{z_o}\right) ,$$

$$R = z\left(1 + \frac{z_o^2}{z}\right) ,$$

$$z_o = \frac{\pi w_o^2}{\lambda} ,$$

$$w = w_o \sqrt{1 + \left(\frac{z}{z_o}\right)^2} ,$$

and $2z_o$ is the confocal beam parameter. Because of the way E_G was defined in Eq. (2.26), $E_G(r)$ has the same form as in Eq. (2.32). For a Gaussian beam, it can also be shown that the total power in the beam is

$$P = \frac{\pi E_o^2 w_o^2}{4}\sqrt{\frac{\epsilon_o}{\mu_o}} \qquad 2.33$$

where E_0 is the electric field at the waist ($z = 0$) and μ_o is the free space permeability. With the above description of Gaussian beams, Eq. (2.29) can now be solved.

For the polarization given in Eq. (2.21a), as in the plane wave case, $\omega_G = \omega_p = \omega_2$ and $k_G = k_p = k_2$. Since it was assumed all the confocal parameters for each beam were the same, the waist sizes cannot be equal for true Gaussian beams. But for $\Delta \ll \omega_1$ and ω_2, the different waist sizes can be approximated as being equal since the two wavelengths, λ_1 and λ_2, are about the same. The procedure for solving Eq. (2.29) is to substitute Eq. (2.20a) in for P_{NL}, first integrate from $r = 0$ to $r = \infty$, integrate again from $z = -\infty$ to $z = \infty$, and finally use Eq. (2.33) to convert the factors of E_0^2 to total power. The result is

$$P_2 = P_{20} \exp [G] \qquad 2.34$$

where p_2 is total power generated at frequency ω_2 if there is initially power p_{20} present,

$$G = -\frac{4\pi^2 N}{\lambda_1 \lambda_2}\sqrt{\frac{\mu_o}{\epsilon_o}}\, \chi''(\omega_2)\, P_1 \quad , \qquad 2.35$$

and p_1 is the power at ω_1. Eq. (2.35) is in agreement with previously[19] published formulas for coherent Raman gain. This is the power expected to be generated in the IRS signal at frequency ω_2 for two overlapping focused Gaussian beams. Just as in the plane wave

case, note that if the exponent, G, is much smaller than unity, the exponential can be approximated as the first two terms in its expansion. The change in power is ω_2 is then

$$\Delta p = p_2 - p_{20} \approx G\, p_{20} \qquad 2.36$$

This approximation is valid for all the experimental results reported in Chapter 5, since G was never any larger than ~ 0.1.

Now consider the polarization expressed in Eq. (2.21b). Again as in the plane wave case, although $\omega_G = \omega_p = 2\omega_1 - \omega_2$, the wave vectors k_G and k_p are not necessarily equal. For the case of a dilute gas with indices of refraction near 1, $\Delta k = k_p - k_G = 2k_1 - k_2 - k_3 \approx$ if the two beams are overlapped without an appreciable crossing angle. The integration over r is again from r = 0 to r = ∞, while the integration over z is from z = - ∞ to z = +∞. Squaring the result and using Eq. (2.33), the final result is

$$p_3 = \frac{16\,\pi^4}{9}\,\frac{\mu_o}{\epsilon_o}\,\frac{N^2|\chi\,(\omega_3)|^2}{\lambda_1^2\,\lambda_2\lambda_3}\,p_1^2\,p_2 \qquad 2.37$$

where p_3 is the total power generated at the frequency ω_3 in a Gaussian beam with about the same size and divergence as the two incident beams at ω_2. Eq. (2.37) can be rewritten in terms of G, using Eq. (2.35), as

$$p_3 = \frac{1}{9}\left(\frac{\lambda_2}{\lambda_3}\right) G^2\, p_2 \qquad 2.38$$

This is the amount of power to be expected in the CSRS signal at frequency ω_3 for Gaussian beams.

Eqs. (2.36) and (2.38) give expressions for the total power generated in the IRS and CSRS signals respectively. Recall that in Section 2.1.2, the polarizations at ω_1 and $\omega_4 = 2\omega_2-\omega_1$ were ignored. Had these polarizations been treated just as the ones at ω_2 and ω_3 were above, two additional equations similar to Eq. (2.36) and (2.38) would have been derived. The only difference between these two additional equations and the expressions in Eq. (2.36) and (2.38) is that the roles of p_1 and p_2 are interchanged and the quantity λ_3 in Eq. (2.38) is replaced with λ_4. The two new versions of Eqs. (2.36) and (2.38) are the SRGS signals at ω_1 and the CARS signal at $\omega_4 = 2\omega_2 - \omega_1$. Both the IRS and SRGS signals are proportional to the product, $p_1\, p_2$. In contrast, the CSRS signal depends on the product $p_1^2\, p_2$, while the CARS signal scales as $p_2^2\, p_1$. Thus the choice of whether to monitor the CSRS signal at ω_3 or the CARS signal at ω_4 is usually made depending on which laser power is larger.

2.1.4 Quantized View of Coherent Raman Scattering

In the previous two sections, both the electric fields and the vibrating molecules have been treated classically. This classical treatment will now be complemented with a brief discussion based on quantized molecules and fields. A quantum mechanical model of a vibrating molecule can be found in Herzberg,[20] while quantized descriptions of the electric fields participating in Raman interactions can be found in Sakurai.[21] The vibrational motion of the molecule is described by a set of energy eigenfunctions and

transitions between different energy levels. Each transition is accompanied by the emission or absorption of two or more photons. The Raman process for a system with two vibrational levels is illustrated in Figure 2-1. The solid horizontal lines represent real vibrational energy levels with the bottom-most level corresponding to the ground state (vibrational quantum number v = 0), while the dotted horizontal lines represent virtual energy levels. The origin of the virtual levels is due to small contributions from higher lying electronic levels. The effective lifetime for a virtual level is typically 10^{-15} sec. Thus the process of Figure 2.1(a), for example, can be visualized as three simultaneous events: emission of a photon at ω_1; absorption of a photon at ω_2; and a molecular transition from v = 0 to v = 1.

In this treatment, the entire ensemble of molecules is assumed to be initially in the ground state. Laser powers are also assumed to be small enough so that all Raman transitions are far from saturated. Thus, the upper level (v=1) can always be approximated as empty, and the process of absorption at ω_1 and emission at ω_2 can be neglected.

All four of the Raman processes mentioned in the previous section are summarized in Figure 2-1. The molecule is driven by two incident fields at ω_2 and ω_1. Both the IRS and SRGS processes are represented by a two-photon transition shown in Figure 2.1(a). While a photon is absorbed at ω_2 and one is coherently (as opposed to spontaneous emission) emitted at ω_1, the molecule simultaneously makes a transition from the ground state to the first excited level. Note that the inverse process is not possible if the upper

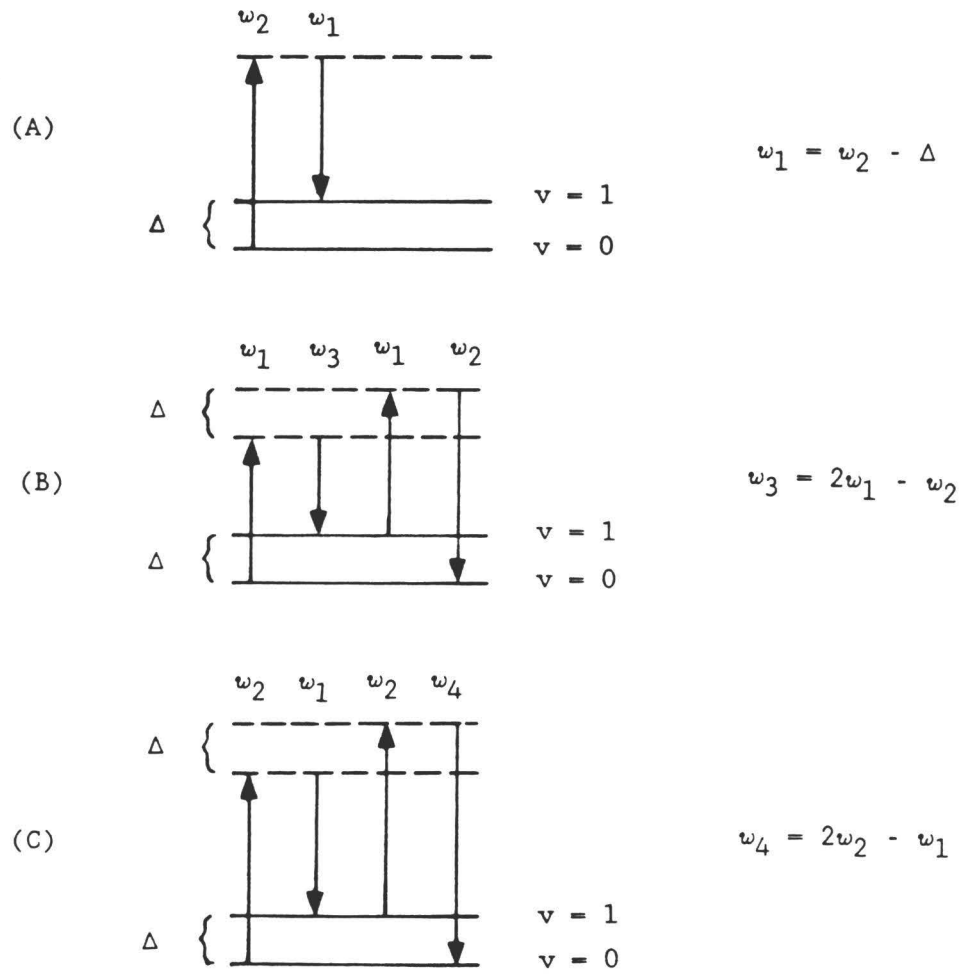

Figure 2.1 Photon Picture for Coherent Raman Scattering. Emitted (Down Arrows) and Absorbed (Up Arrows) Photons are Shown for (a) SRGS if ω_2 is the pump and IRS if ω_2 is the probe, (b) CSRS and (c) CARS.

population always remains much less than that in the ground state. Thus there is an increase (gain) in photon energy at ω_1 and a decrease (loss or absorption) in photon energy at ω_2. The four photon CSRS process in Figure 2.1(b) is a simultaneous emission of a photon at ω_3, emission of a photon at ω_2, and an absorption of two photons at ω_1. Unlike the IRS/SRGS process, the CSRS interaction does not result in a transition between energy levels for the molecule. This CSRS process is also a resonance effect that occurs when $\omega_2 - \omega_1 \approx \Delta$. Finally, the CARS process is also a four photon process that results in the generation of a new field at ω_4, as shown in Figure 2.1(c).

The magnitude of the signals generated at ω_2 and ω_3 were given in Eqs. (2.36) and (2.38). The diagram in Figure 2.1(a) shows that the photons at frequency ω_2 are being absorbed and so Eq. (2.36) is interpreted as the magnitude of the absorption of the field at ω_2. Similarly, the diagram in Figure 2.1(b) shows photons being emitted at ω_3 and so Eq. (2.38) is just the magnitude of the field generated at ω_3. The CSRS process also generates photons at ω_2, but for $G \ll 1$ the number of these emitted photons is small compared to the number absorbed at ω_2 due to the IRS process. So, under the conditions described in this section, the IRS and CSRS processes can be approximated as independent and non-competing processes. The same conclusion also holds for the SRGS and CARS signals.

2.2 Doppler Effect in Coherent Raman Spectroscopy

The main idea behind measuring a velocity using coherent Raman spectroscopy is to measure the velocity dependent Doppler frequency

shift of a Raman line. In this section, the Doppler shift's velocity dependence will be described. First the Doppler shift for a single photon emission (or absorption) will be reviewed. Next this idea will be expanded to cover the two photon IRS and four photon CSRS interactions. Discussion of the frequency resolution and quantities (pressure broadening, laser linewidths, etc.) which affect it will be delayed until the results are presented in Chapter V.

Consider an atom or molecule moving with velocity, $\vec{v}$, along the line of sight and away from the stationary observer (or detector) as shown in Figure 2.2(a). If the atom radiates with frequency ν_o in its own frame or reference, the frequency ν measured by the stationary observer is lower than the ν_o measured by an observer moving with the molecule. This is the first order Doppler shift; the relation between ν and ν_o is

$$\nu = \nu_o - (\frac{v}{c})\ \nu_o \quad .$$

Similarly, if the atom is moving towards the detector, the stationary observer will measure frequency

$$\nu = \nu_o + (\frac{v}{c})\ \nu_o \quad .$$

This effect also occurs for the absorption of light by molecules moving with respect to the source of light. An atom with resonant absorption frequency ν_o will absorb light at frequency $\nu = \nu_o - (\frac{v}{c})\ \nu_o$ if moving away from the light source and absorb at $\nu = \nu_o + (\frac{v}{c})\ \nu_o$ if moving towards the light source.

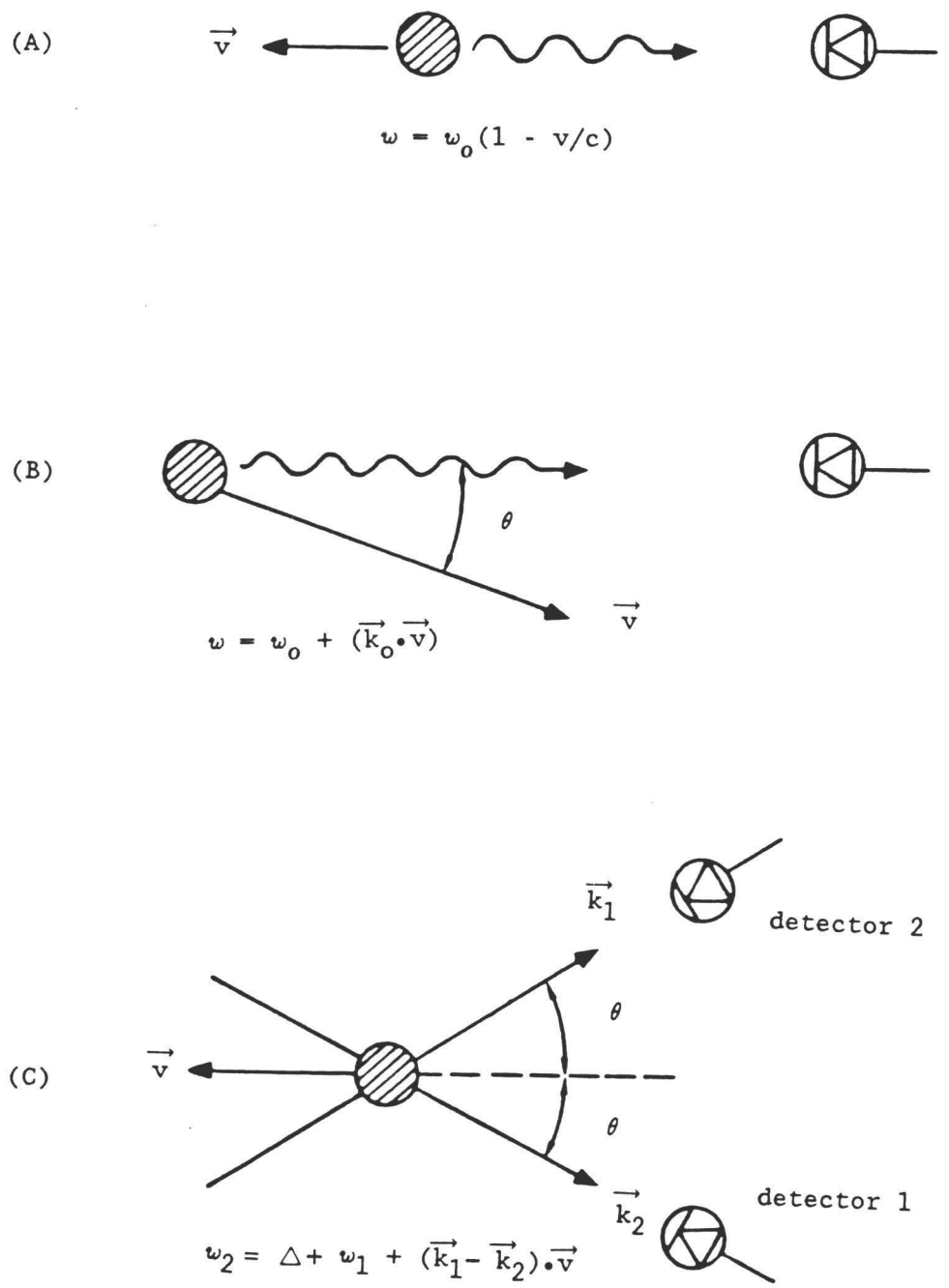

Figure 2.2 First Order Doppler Effect in Raman Scattering. Single-photon (A) collinear and (B) non-collinear spontaneous fluorescence and (C) two-photon stimulated Raman scattering are illustrated.

Now consider the situation shown in Figure 2.2(b) where the atom is moving at an angle θ with respect to the line of sight to the detector. Here it is only the velocity component, v cos θ, along the line of sight that contributes to the first-order Doppler shift. Defining the wave number as $\vec{k}_o = (2\ell/\lambda_o)\,\hat{u}$, where $\hat{u}$ is the unit vector along the direction of propagation, the detected angular frequency is $1 = \omega_o + \omega_o(\frac{v\cos\theta}{c}) = \omega_o + k_o\, v\cos\theta$. This result can also be written

$$\Delta\omega = \vec{v} \cdot \vec{k} \quad , \qquad 2.39$$

where $\Delta\omega \equiv \omega - \omega_o$ is the single photon Doppler shift.

Next consider a molecule (with an internal vibrational energy, $\hbar\Delta$) that participates in a two photon interaction with the geometry shown in Figure 2.2(c). The energy level diagram for this process is shown in Figure 2.1(a), which depicts a simultaneous absorption of a photon at ω_2 and an emission of a lower energy photon at ω_1. The molecule is simultaneously excited to an energy level $\hbar\Delta$ above the initial level. This is a resonant process which occuurs when

$$\omega_2 - \omega_1 = \Delta \quad . \qquad 2.40$$

If this molecule is moving towards the source at ω_1, the molecule sees the fields at ω_1 shifted to $\omega_1 + \vec{v} \cdot \vec{k}_1$. If a Raman transition occurs, the molecules radiates at $\omega_1 + \vec{v} \cdot \vec{k}_1 + \Delta$ in its own frame of reference. Since the molecule was traveling away from the detector during this emission, the radiated field is red shifted to $\omega_2 = \omega_1 + \Delta + \vec{v} \cdot \vec{k}_1 - \vec{v} \cdot \vec{k}_2$. The net result is that the transition

is shifted from the condition given in Eq. 2.40 by the amount of

$$\Delta\omega = (\vec{k}_1 - \vec{k}_2) \cdot \vec{v} \qquad 2.41$$

This is the first order Doppler shift in the Raman resonance, which has the same magnitude whether the loss at ω_2 or the gain at ω_1 is monitored. To summarize, a molecule with zero velocity with respect to the laser sources exhibits a Raman gain/loss resonance when $\omega_2 - \omega_1 = \Delta$; when the molecule is moving with velocity v, the Raman resonance shift is given by Eq. 2.41. Since Eq. 2.41 is a vector equation, it is valid for any combination of directions for v, k_2, and k_1 in Figure 2.2(c).

The Doppler shift of the CARS or CSRS processes is also given by Eq. 2.41. A four photon process as shown in Figure 2.1(b) can be regarded as two simultaneous two-photon events, where the Doppler shift for each two-photon process can be deduced just as above. The resultant Doppler shifts for both two-photon events are identical and given by Eq. 2.41. Thus, Eq. 2.41 relates the velocity of a molecule to its Doppler shift for both the IRS and the CSRS effects. In thermodynamic equilibrium, a large number of molecules will have a standard Maxewell-Boltzman velocity distribution. Using this distribution of velocities in place of v in Eq. 2.41 will generate a distribution of Doppler shifts which yields the usual Doppler broadened profile. If there is an average flow velocity, V, superimposed on the thermal distribution, this velocity can be determined by measuring the average frequency shfit predicted in Eq. 2.41.

2.3 Energy Level Population Distributions in Diatomic Molecules

In this section the basic ideas of temperature and density measurements with coherent Raman spectroscopy are described. This discussion is oriented towards diatomic homonuclear molecules which are in thermodynamic equilibrium. For a large ensemble of identical molecules in thermodynamic equilibrium, the relative number of molecules in a given state r is

$$P_r = \frac{e^{-\frac{E_r}{k_B T}}}{\sum_r e^{-\frac{E_r}{k_B T}}} , \qquad 2.42$$

where E_r is the energy of the state r, k_B is Boltzman's constant, and the sum is over all possible states. The total internal energy of a single molecule consists of the sum of the binding energy of the electrons, the vibrational energy of the two nuclei, and the rotational energy of the molecule. For diatomic nitrogen at room temperature or below, E_r for the first vibrational (or electronic) state is large compared to the thermal energy and there is essentially zero population in the excited vibrational and electronic states. Room temperature does correspond to enough thermal energy to substantially populate the first several rotational energy levels. This allows a measurement of temperature by measuring the rotational energy level distribution and comparing it to Eq. 2.42.

Application of Eq. 2.42 to the rotational energy levels of an ensemble of diatomic molecules yields a rotational state population density distribution of

$$N_J \propto \frac{N_v\, g_J (2J + 1)\, e^{-\frac{B\, J(J+1)\, hc}{k_B T}}}{\sum_J g_J (2J + 1)\, e^{-\frac{B\, J(J+1)\, hc}{k_B T}}} . \qquad 2.43$$

Here N_J is the number of molecules per unit volume with rotational quantum number J, and B is the rotational constant as defined in Reference 20. N_v is the total number density of the vibrational level. The factor of (2J + 1) is due to a degeneracy of rotational levels, while the factor g_J is due to a degeneracy which arises because of the spins of the two nuclei. For nitrogen (with nuclear spin of 1), g_J is 3 for odd J states and is 6 for even J states. The IRS signal strength for any line in the Q-branch is proportional to N_J. Q-branch transitions are those for which the rotational quantum number remains unchanged, i.e. $\Delta J = 0$. Using Eq. (2.43), the relative signal strength (or populations) of two different J states is

$$\frac{N_J}{N_{J'}} = \frac{(2J+1)\; e^{-BJ(J+1)hc/k_BT}}{(2J'+1)\; e^{-BJ'(J'+1)hc/k_BT}} \quad , \qquad 2.44$$

where J and J' are the rotational quantum numbers of the two different rotational states. Thus, Eq. (2.44) can be used to determine the temperature if the relative heights of two or more rotational lines from the Q-branch IRS spectrum are known. To determine the rotational temperature with a CSRS experiment, the relative strengths of the separate rotational lines must be equated to $(N_J/N_{J'})^2$, since the CSRS signal is proporational to the square of the density.

The total density N_v of the gas sample is proportional to the integrated intensity for the entire Q-branch, which is proportional to the total area under the curve for all the substantially populated rotational levels. Thus an absolute measurement of density requires the determination of the signal strength of each rotational line. If

the temperature of the sample and the fraction of molecules in state J are already known, the total density N_v can then be determined from the integrated intensity (or area under the curve) of a single rotational line. The constant of proporationality can be eliminated by making the measurement relative to a known density. Thus coherent Raman scattering can also be used to measure an unknown density relative to a known density using only one rotational line in the Q-branch.

A couple of comments about these kinds of temperature and density measurements are in order. The temperature determined by the above method is actually the rotational temperature and is only equal to the translational (or vibrational) temperature if the sample is in thermodynamic equilibrium. For nuclear spin 1 nitrogen molecules, collisional transitions between odd J rotational states and even J rotational states are strongly forbidden[22] due to symmetry considerations. Thus the molecules in odd J states change their population distribution independently from those in the even J states for time periods that are short compared to the time to reach equilibrium. Thus at extremely low temperatures (10 K for N_2), where only J = 0 and 1 are appreciably populated, the population distribution is not described by Eq. (2.44) and the temperature measurement described here is no longer valid. Since the measurements reported in this work were always above 100 K, this effect is ignored.

CHAPTER 3

One-Dimensional Supersonic Flow in a Pipe

The purpose of this chapter is to present a cursory overview of a one-dimensional supersonic flow in a closed duct. A detailed account of the summary given here can be found in the standard texts.[23-26] The one-dimensional model assumes the flow parameters (i.e., velocity, temperature, or density) change only as a function of a distance along the pipe axis but not in the direction perpendicular to the flow. Thus the values obtained with this model are to be taken as averages of the values across the cross sectional area for any given point along the pipe axis. It will also be assumed that there is no heat flow through the walls of the pipe. In section 3.1 the results of purely isentropic (i.e. adiabatic and reversible) flow will be presented. This means the viscous drag effects (i.e. friction) with the walls are neglected. In section 3.2, this viscous interaction is included for the constant area portion (test section) of the pipe, although for simplicity, it is still ignored in the converging-diverging (nozzle) portion of the pipe. The results of these two sections are equations which predict the average velocity, temperature, and density as a function of position along the pipe axis for both isentropic (frictionless) and viscous one-dimensional flow models.

The primary motivation for this chapter was to help with the design and construction of the miniature supersonic wind tunnel. It will also be interesting to compare the quantitative results obtained with the formulae in this chapter to the experimental results in Chapter 5. However, exact agreement between the theoretical results of this chapter and the experimental results of Chapter 5 should not be expected. The one-dimensional (no radial dependence) nature of the theory, the empirical method of including viscous effects, and the uncertainty in the friction coefficient will all contribute substantial uncertainties in the model.

3.1 Isentropic Supersonic Flow

The main idea behind generating a supersonic flow in a duct is that supersonic flow can only be generated in a diverging (increasing cross-sectional area) duct which is preceeded by a converging section. Hence it is of interest to describe the flow in a pipe similar to that shown in Fig. 3.1. The pipe connects the two large reservoirs at pressures of P_o and P_b. Reservoir 1 is at temperature T_o, density ρ_o, and has negligible velocity. The section AC is hereafter called the nozzle while the section CD is referred to as the test section. If $P_b < P_o$, flow is induced through the nozzle into Reservoir 2. No matter how large the pressure ratio P_o/P_b, supersonic flow can never be generated in the converging portion AB. When the ratio P_o/P_b reaches

$$\frac{P_o}{P_b} = \left(1 + \frac{\gamma-1}{2}\right)^{\frac{\gamma}{\gamma-1}} , \qquad 3.1$$

Figure 3.1 Converging-Diverging Nozzle Used to Generate Supersonic Flow. If $P_b \ll P_o$, the flow is accelerated to Mach 1 and cooled to 0.833 T_o at plane B. In the diverging section (BC) the flow is accelerated to $M > 1$ and further cooled. The Mach # at plane C depends only on the diameter ratio D_C/D_B. For isentropic flow (i.e. neglible friction) the velocity, temperature, and pressure will be constant throughout the test section (CD). A shock wave at plane D returns the fluid to the pressure (P_b), temperature (T_o), and velocity (~ 0) of reservoir 2.

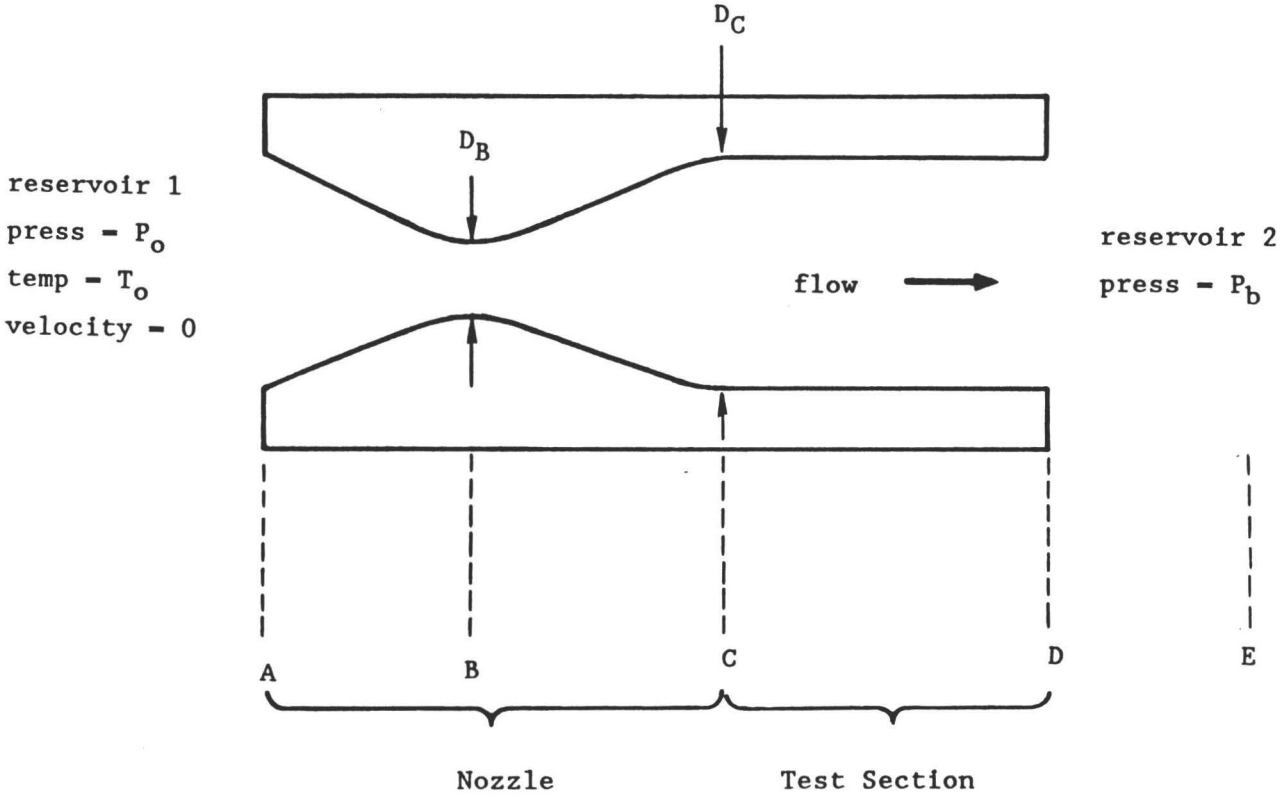
D_C
D_B
reservoir 1
press = P_o
temp = T_o
velocity = 0
flow
reservoir 2
press = P_b
A
B
C
D
E
Nozzle
Test Section

where γ is the ratio of specific heat at constant pressure to that at constant volume, the flow at the throat (plane B) reaches sonic velocity. As P_o/P_b becomes larger than that given in Eq. (3.1), supersonic flow is generated in the diverging portion BC. For sufficiently large values of P_o/P_b, the entire diverging section BC and the constant area test section produce supersonic flow.

Under the condition $P_b \ll P_o$, the supersonic Mach number M at any point downstream of plane B is related to the ratio of the cross-sectional area A at the same point to the minimum cross sectional area A_B by the following relation:

$$\frac{A}{A_B} = \frac{1}{M}\left[\frac{2}{\gamma+1}\left(1 + \frac{\gamma+1}{2} M^2\right)\right]^{\frac{\gamma+1}{2(\gamma-1)}} \quad . \tag{3.2}$$

The temperature T, pressure P, and density ρ at any cross-sectional plane in the nozzle are given in terms of P_o, T_o, P_o, and M as:

$$P = P_o \left[1 + \left(\frac{\gamma-1}{2}\right) M^2\right]^{\frac{\gamma}{1-\gamma}} \tag{3.3}$$

$$T = T_o \left[1 + \left(\frac{\gamma-1}{2}\right) M^2\right]^{-1} \tag{3.4}$$

$$\rho = \rho_o \left[1 + \left(\frac{\gamma-1}{2}\right) M^2\right]^{\frac{1}{1-\gamma}} \quad . \tag{3.5}$$

Finally, the velocity v at any point is simply

$$v = M\, v_s \quad , \tag{3.6}$$

where the speed of sound is

$$v_s = \sqrt{\gamma k_B T/m_o} \quad . \qquad 3.7$$

The quantities k_B and m_o are the Boltzman constant and the molecular mass respectively. Eqs. (3.3) through (3.7) give the average pressure, temperature, density, Mach number, and velocity for any point in the nozzle in terms of the ratio A/A_B and the parameters of Reservoir 1. If friction is negligible, then the flow parameters are constant throughout the constant area test section and equal to those at plane C.

3.2 Viscous Effects in a Constant Area Pipe

To simplify matters, frictional effects in the nozzle are neglected, and only taken into account for the constant area test section. In a one-dimensional model, the friction effects are added in an empirical manner which allows the calculation of an average velocity (or temperature, etc.) associated with any point along the axis of the tube. The radial gradients in the flow parameters are still ignored. The viscous effect in the test section is described by a quantity known as the friction coefficient f, which is defined as the ratio of wall shear stress to the inertial force per unit area of the flowing stream. Friction coefficients are seldom calculated from first principles and are usually measured for each individual flow geometry.

To include friction in a one dimensional model, it is assumed the supersonic flow parameters at the entrance (plane C in Fig. 3.1) to the constant area test section are known. The velocity and Mach number are slowly reduced, due to friction, as a function of axial

distance down the test section. The supersonic flow is eventually slowed to a sonic (M = 1.0) condition at plane E. The physical pipe does not have to be as long as the distance CE; and short enough pipes (as illustrated in Fig. 3.1) will maintain supersonic flow over their entire length. At any arbitrary point, P, in section CD, the distance L_p to plane E is related to the Mach number M_p at point P by

$$L_p = \frac{D}{4f} \left\{ \frac{1 - M_p^2}{\gamma M_p^2} + \frac{\gamma+1}{2\gamma} \ln \left[\frac{(\gamma+1)M_p^2}{2\left(1+(\gamma-1)\frac{M_p^2}{2}\right)} \right] \right\} , \qquad 3.8$$

where D is the pipe diameter, and f is the friction coefficient. At two arbitrary points in the test section, the length L between them is given by

$$L = L_1 - L_2 , \qquad 3.9$$

where L_1 and L_2 are given by Eqn. (3.8). In this manner the Mach numbers M_1 and M_2 at two arbitrary points can be related. Thus if the entrance Mach number is known then the Mach number at any point in the test section can be calculated using Eqns. (3.8) and (3.9).

When frictional effects are included, the temperature and pressure in any cross sectional plane of the test section can be related to the Mach number M at the same plane with the relations:

$$\frac{P}{P_E} = \frac{1}{M}\sqrt{\frac{\gamma+1}{2\left[1+\frac{\gamma-1}{2}M^2\right]}} \qquad 3.10$$

$$\frac{T}{T_E} = \frac{\gamma + 1}{2\left[1 + \frac{\gamma-1}{2}M^2\right]} . \qquad 3.11$$

The quantities T_E and P_E are the values at the plane where the Mach number has been reduced to exactly one. Using Eq. (3.10) twice, once to relate M_1 to P_1 and a second time to relate M_2 to P_2, P_E is eliminated and the pressure ratio at any two planes is related to the Mach numbers at these two planes. The same argument holds for temperatures and Eq. (3.11). Thus if the pressure and temperature are known at the entrance to the test section, Eqs. (3.8) through (3.11) can be used to calculate the pressure and temperature at any point in the test section.

CHAPTER 4

Experimental Apparatus

The motivation for the experimental design and choice of laser systems is first described in section 4.1. Then an overview of the entire experiment is outlined in section 4.2. Details of the two different lasers are covered in sections 4.3 (pump laser) and 4.4 (probe laser). Finally the detection electronics and the supersonic wind tunnel are described in Sections 4.5 and 4.6 respectively.

4.1 Experimental Design Considerations

The basic design of this experiment is governed by two important restrictions. First, stimulated Raman signals, which depend on the third order susceptibility, are generally small and require large laser intensities to obtain easily observable signals. Consequently, high peak powers (KW to MW range) are usually used in stimulated Raman experiments. Secondly, the expected Doppler shifts due to typical wind tunnel velocities (500 m/s) vary from 1.0 GHz to 100 MHz, depending on the geometry of the scattering process. Thus narrow bandwidth lasers are also necessary. The high peak power and narrow bandwidth coherent light source necessary for this experiment was obtained with the cw oscillator and pulsed amplifier system that is described in section 4.3.

However, in experiments[27] preliminary to the present work, flow velocity measurements were demonstrated with a wide bandwidth (6 GHz) laser. This was possible only because of the backward scattering (counter propagating laser beams) geometry, which provided the maximum possible Doppler shift for a given velocity (see Figure 2.2). The velocity measurements were made with densities of 10^{19} cm^{-3}, where the signal-to-noise ratio of the Raman spectra was about 5.

However, one goal of this current work is to measure supersonic flow parameters under conditions similar to those in a typical full-scale wind tunnels. Many full-scale wind tunnels produce supersonic N_2 flows with pressures of 50 torr, temperatures of 150 K, and densities of 10^{18} cm^{-3}. For these conditions, the counter propagating geometry gives a Doppler linewidth component (2 GHz) that is 10 times the collisional linewidth component (200 MHz). Because the stimulated Raman signal is inversely proportional to the total linewidth (Eqn. 2.22), the signal from 10^{18} cm^{-3} of N_2 is much smaller if a counter-propagating geometry (and maximum Doppler linewidth) is chosen for the two laser beams. In contrast, a forward scattering geometry (co-propagating laser beams) gives a Doppler linewidth contribution of 150 MHz and increases the strength of the Raman signal to the point that it can be readily observed. But the co-propagating geometry also yields 15 times less Doppler shift and hence the narrow bandwidth laser of section 4.3. is necessary to observe these small Doppler shifts (~ 100 MHz).

4.2 Overview

An overview of the entire experiment is shown in Figure 4.1. The cw argon-ion laser (ω_2) and the pulsed dye laser (ω_1) supply the electric fields at frequencies ω_2 and ω_1 that are discussed in Chapter 2. These two beams are collimated, overlapped, and focussed into the high speed flow region using a co-propagating geometry. After the flow region, the three beams are recollimated and spectrally dispersed with a prism. The beam at 6767 Å corresponds to the coherent Stokes Raman scattering (CSRS) signal at ω_3 (Eq. 2.38). The inverse Raman scattering (IRS) signal at ω_2 (Eq. 2.36) is an attenuation of the beam at 5145 Å, that is detected with the IRS signal diode. The IRS reference diode also monitors a portion of the 5145 Å beam. The voltage from the reference diode is subtracted from the voltage of the signal diode to reduce the noise arising from power fluctuations of the 5145 Å beam.

Using telescopes in each beam, both the dye and argon-ion laser beams were collimated as well as possible over distances of a couple of meters. Both beam diameters were about 3 mm as measured by ruler and eye on white cards. For the argon-ion beam, which is close to a TEM_{oo} mode, this corresponds to a beam radius (beam intensity down by a factor of $1/e^2$) of about 30 μm in the focal plane. After collimation, the two beams were spatially overlapped using a CVI dichroic mirror which has 60% transmission at 5145 Å and 99% reflectivity at 5845 Å. The beams are then focused into the flow region using a 10 cm focal length lens as shown in Figure 4.1. Under these conditions, and assuming diffraction limited Gaussian beams, the confocal parameter was about 4 mm. Thus all of the coherent Raman signals are

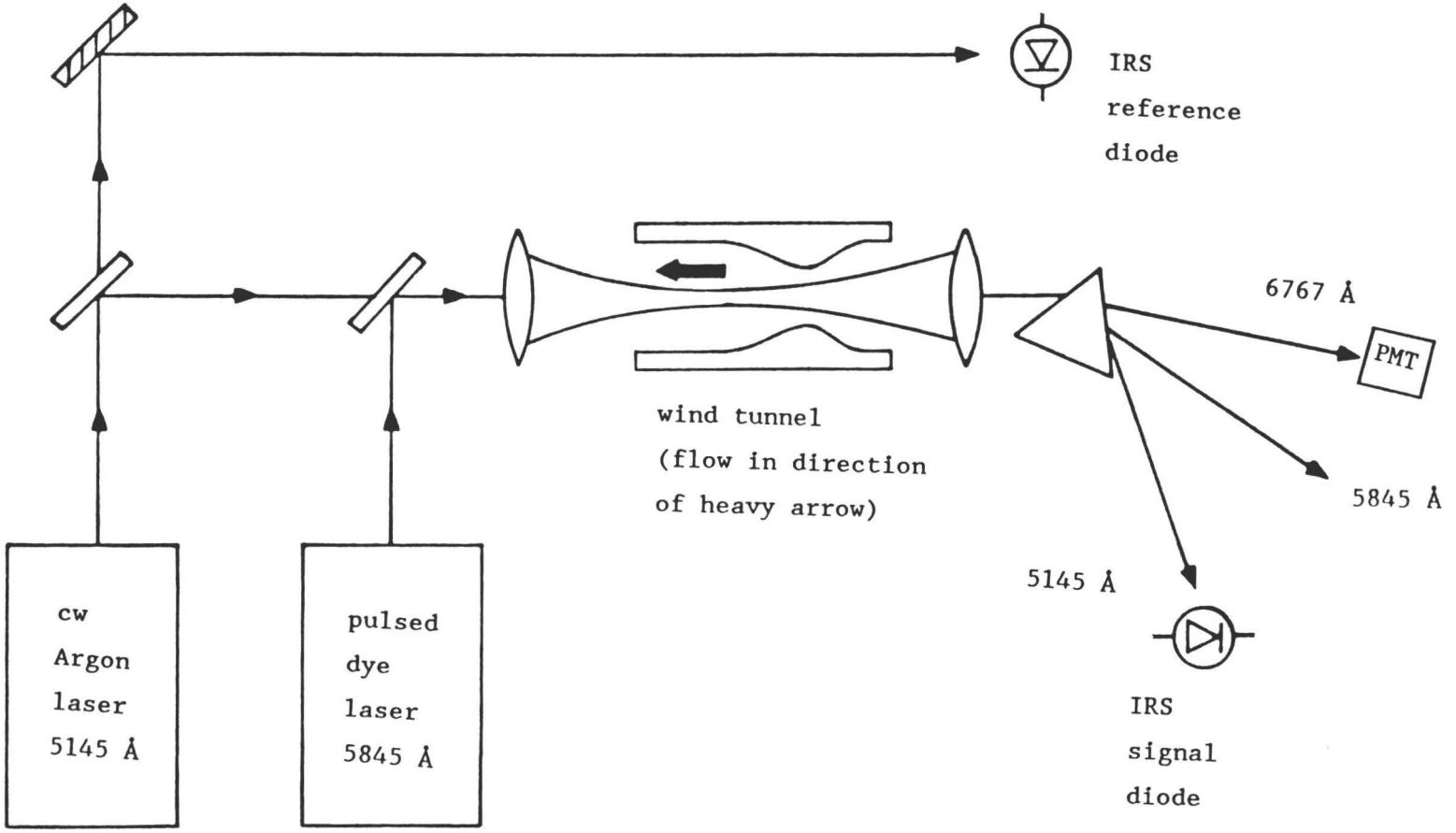

Figure 4.1 Experimental Overview for Velocity Measurements Using Inverse Raman Spectroscopy.

generated entirely within the high speed N_2 flow region which is 3 mm wide by 25 mm long. The resonances are frequency shifted according to the two photon Doppler shift described in Section 2.2.

4.3 The Pump Laser

A high peak power, narrow bandwidth laser was constructed by amplifying the output of a commercial cw dye laser with a series of amplifiers that are pumped with a commercial pulsed Nd:YAG laser. This system is similar to one previously reported in the literature.[28]

The initial laser oscillator for the pump laser is a tunable single mode cw dye laser which is pumped with an argon-ion laser. The dye laser is a Coherent model 599-21 which is actively stabilized to an average linewidth of 1 MHz. It is operated at a wavelength close to 5845 Å, where it typically produces between 50 and 100 mW depending on the state of the optical alignment. Most of the output power is sent to an optical amplifier chain, while the remaining 10% is used for diagnostics including an I_2 saturation spectroscopy set-up. The diagnostics include a scanning confocal Fabry-Perot interferometer (Tropel, Inc. model #240) to verify single mode operation of the laser, a Kowalski-type wavemeter[29] which reads the cw dye laser wavelength to 1 part in 10^6, and a temperature stabilized (± 0.001 C) confocal interferometer with a free spectral range that was known to be 74.295 ± .0003 MHz (far more accurate than necessary for the present velocity measurement). This interferometer was built and calibrated by Louis Hlousek[30] and was used to calibrate

the frequency splittings of the I_2 hyperfine transitions obtained from the I_2 saturation spectroscopy experiment.

Saturation spectroscopy is a standard[31] technique for obtaining high resolution spectra of molecules by eliminating the Doppler broadening. The setup is illustrated in Figure 4.2. A small portion of the cw dye laser beam is split into two beams with a beam-splitter. These two beams are focussed (30 cm lenses) and crossed in the I_2 cell in a counter propagating geometry. The crossing angle is about 1.0 deg. One beam (the pump) is chopped at 1 kHz with a mechanical chopper, while the second beam (the probe) is monitored with a photodiode. In the absence of the chopped pump beam, tuning the frequency of the dye laser through an I_2 transition would produce a Doppler broadened absorption in the intensity of the probe beam. With the addition of the chopped pump beam, a much smaller Doppler free absorption signal, which is in phase with the chopping of the pump beam, is also produced. This phase correlated signal is then detected with a lock-in amplifier as shown in Figure 4.2. At room temperature I_2, this technique gives a resolution of the hyperfine structure with linewidths of less than 10 MHz. These hyperfine lines are used as frequency markers for measuring the Doppler shifts of the Raman lines.

To increase the tunable dye laser power, it is pulse amplified using dye cells pumped with a frequency doubled YAG laser as shown in Figure 4.3. The cw dye laser beam is focused in both of the first two stages, then collimated to a 3 mm diameter beam in the third and final stage. A direct vision prism and 100 μm pinhole are used to help eliminate broadband spontaneous fluorescence emitted in the

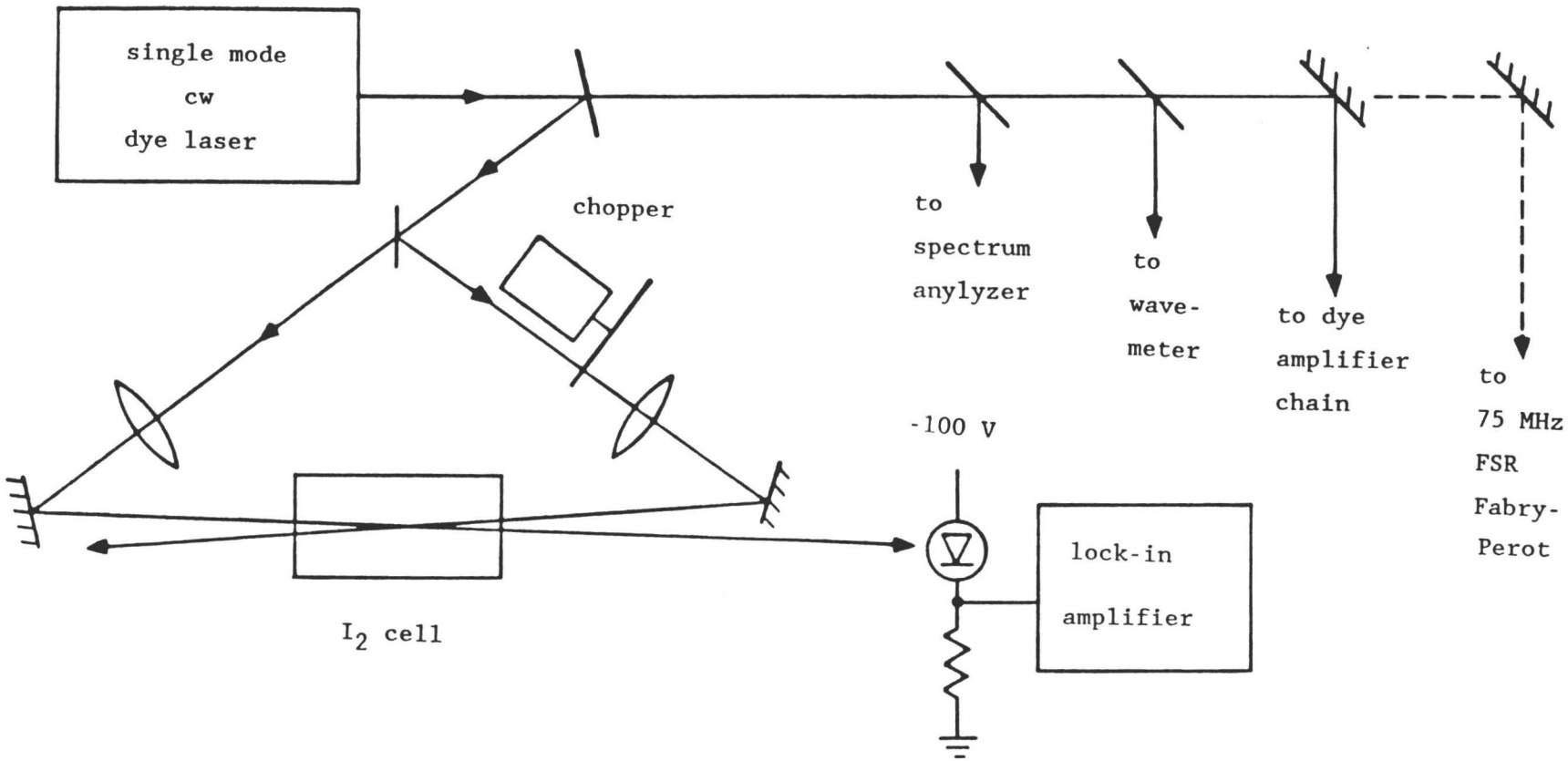

Figure 4.2 Schematic of Saturation Spectroscopy in I_2.

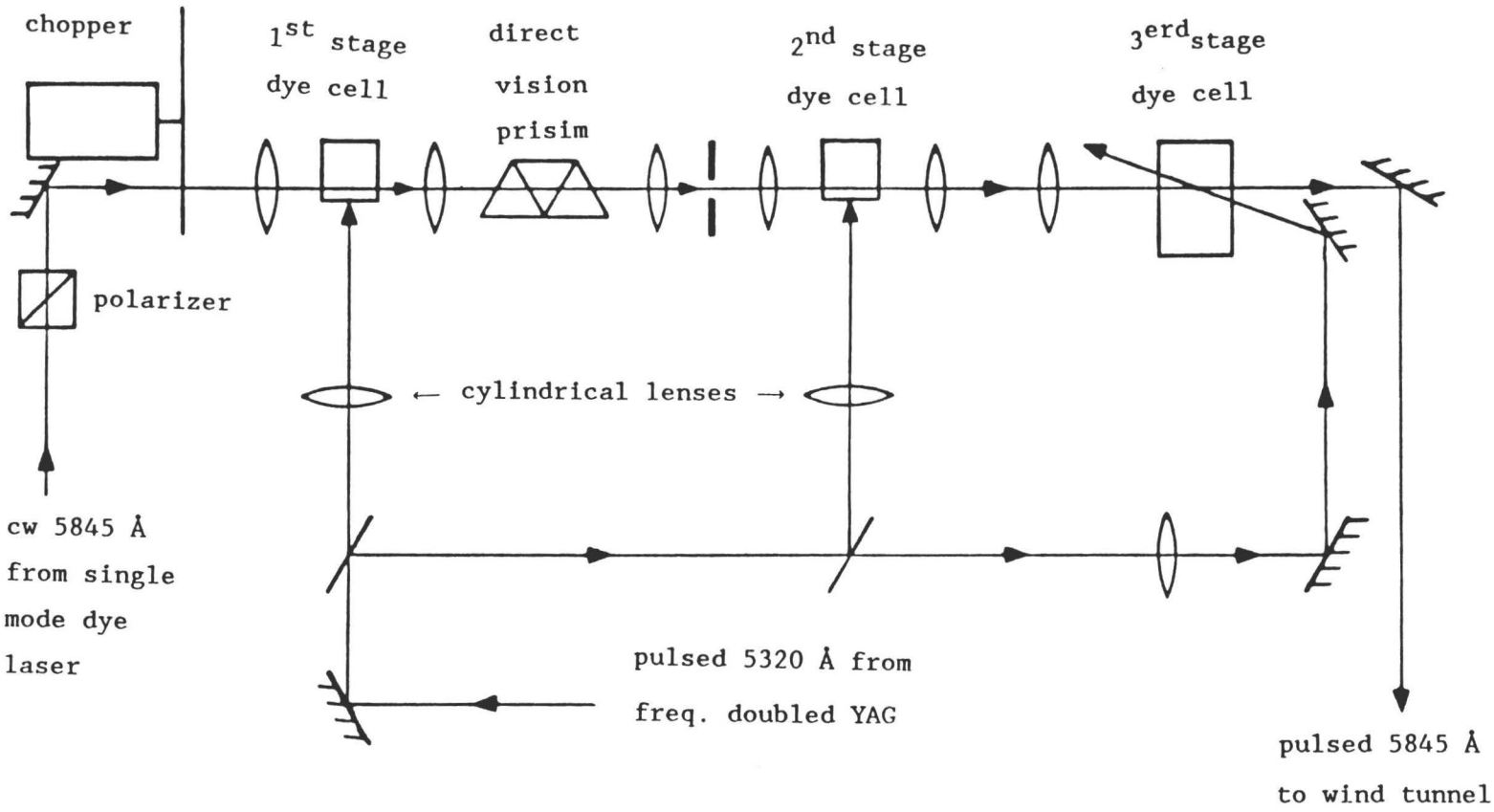

Figure 4.3 Schematic of Dye Laser Amplifier Chain.

first stage from being amplified in the second stage. Backscattered emission from the amplifier chain can ruin the performance of the frequency locking servo loops in the cw dye laser. But this backscattered emission also has a large divergence. Therefore, the first amplifier stage was located 4 m away from the cw laser, which greatly reduced the backscattered emission entering the laser. A polarizer between the cw laser and the first amplifier stage also reduced the backscattered emission into the cw laser, since the backscatter was not polarized to a large degree.

The Nd:YAG laser is a frequency doubled Quanta-Ray model DCR-1A which produces 6-7 nsec pulses at 5320 Å. This laser is operated at a 10 Hz repetition rate, and produces 50 to 70 mj/pulse that is necessary to pump the three dye cells (depending on the relative alignment of the dye and YAG beams). About 5% and 15% of the total YAG output is used to transversely pump the first and second stages respectively. The remaining YAG power is used to longitudinally pump the third stage. Since the YAG laser produces nanosecond pulses at 10 Hz, the cw dye laser beam is mechanically chopped to reduce thermal heating of the dye in the first stage between YAG pulses. After chopping, the dye laser beam that enters the first amplifier stage consists of a 1 ms pulse at 10 Hz. The YAG is then triggered off the mechanical chopper to fire in the middle of the dye laser pulse. The final tunable output from the third stage is approximately 5 nsec pulses at 10 Hz with 1 to 2 MW of peak power depending on the age of the dye. Variations of the peak intensity were measured with a fast photodiode and oscilloscope. The typical pulse-to-pulse variations were about 20%. The final linewidth was nearly Fourier transform

limited and measured to be about 100 MHz. This was accomplished by directing some of the pulsed output into a Tropel model 240 spectrum analyzer and tuning the dye laser across an etalon peak. An example of the pulsed dye laser lineshape is shown in Figure 4.4. This cw oscillator-pulsed amplifier produces a narrow frequency bandwidth, high peak power, tunable dye laser, and will be referred to as the pump laser from now on.

4.4 Probe Laser

The second of the two lasers necessary for this coherent Raman experiment is the probe laser. It is a Coherent model CR-3 argon-ion three watt laser that uses a prism inside the cavity to select only the 5145 Å transition. A temperature stabilized etalon is then introduced into the cavity which confines the lasing to a single longitudinal mode. This yields a linewidth of about 10 MHz which arises because of mechanical fluctuations of the resonator. The linewidth was determined by putting a small fraction of the laser output into a Tropel model 240 spectrum analyzer and tuning the laser across an etalon peak. The argon-ion linewidth was measured to be about 10 MHz, which is negligible compared to the 100 MHz linewidth of the pump laser. Thus the linewidth of the experimental apparatus is determined by the pump laser and is about 100 MHz. However, the frequency of the Argon-ion probe laser continually drifts with time. This frequency drift, due to slow temperature fluctuations, was measured to be typically 20 MHz over a 10 min. period. Drifts as large as this would severely affect a 10 min measurement of a 100 MHz Doppler shift.

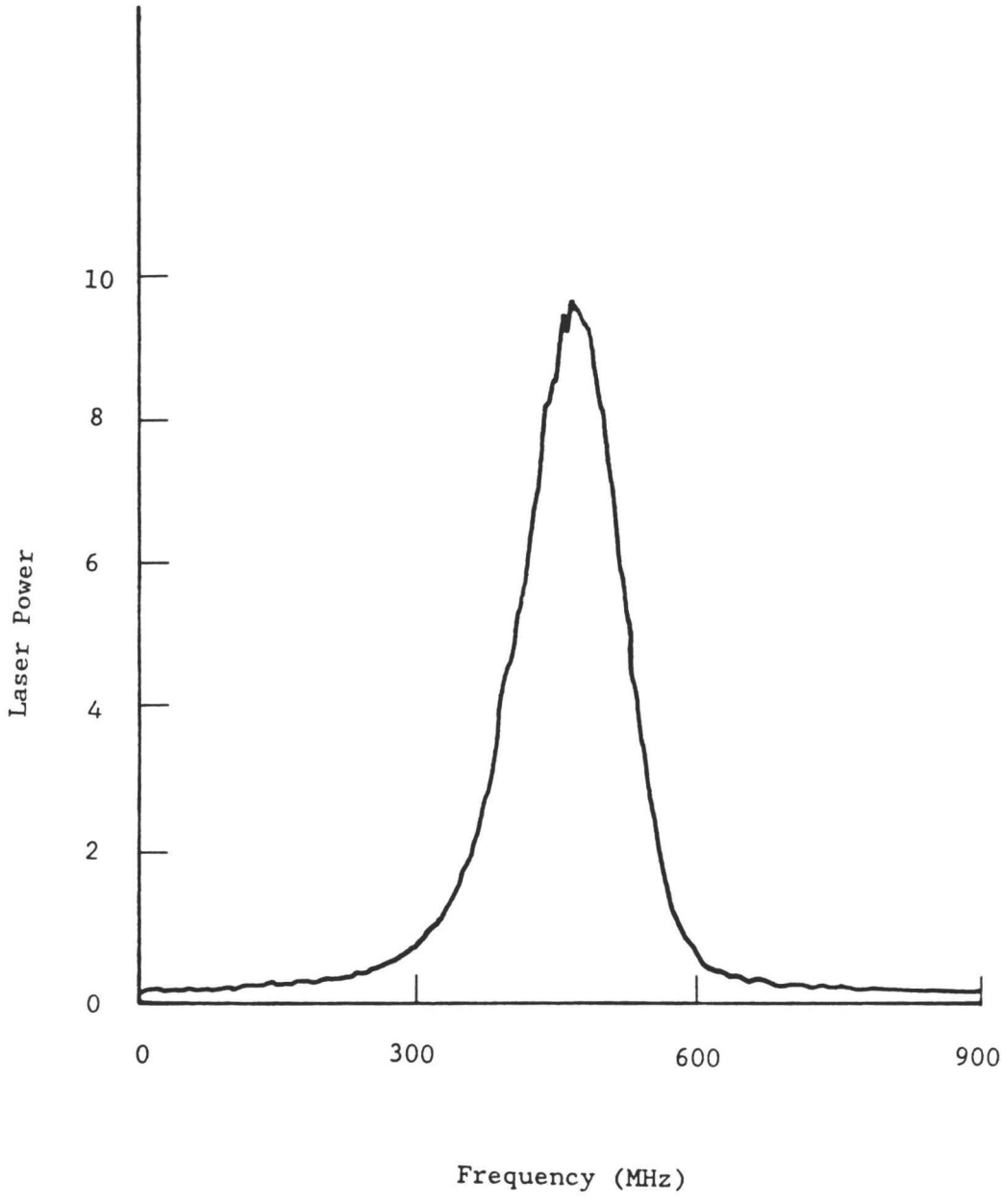

Figure 4.4 Typical Lineshape Observed for the Output of the Pulsed Dye Laser. The spectrum analyzer used to obtain this profile has a bandwith of 7 MHz.

Thus, the argon-ion laser was stabilized against these long term drifts by locking the laser frequency to the side of a Doppler broadened I_2 transition which overlaps the tuning range of the argon-ion laser. This locking technique is illustrated in Figure 4.5. The fluorescence of the I_2 line was monitored with a photomultiplier tube, while the total power output of the laser was monitored with a photodiode. The difference of the photomultiplier and diode voltage signals was amplified, integrated, and applied to a piezo-electric crystal (PZT) which was attached to the output mirror of the laser. The differences of the photomultiplier and diode voltages was used to prevent the locking loop from inadvertently shifting the frequency when the laser output power changed. To lock the laser frequency to the I_2 fluorescence signal, the laser frequency was manually tuned halfway up the side (where the slope is the steepest) of the I_2 fluorescence line; then the feedback loop was activated. In this manner, the argon-ion laser was actively locked to the side of the I_2 line. Because the error voltage that is applied to the PZT is the difference of the I_2 fluorescence (photomultiplier) voltage and the argon-ion power (diode) voltage, this locking technique keeps the laser frequency stable in spite of output power changes in the laser. The response time of the feedback looped was estimated to be about 0.3 s. Thus the stabilization loop can reduce only the slow thermal drift in the argon-ion laser and is too slow to reduce the faster (KHz or more) mechanical fluctuations. The probe laser was monitored with a homemade spectrum analyzer to verify that it remained single mode at all times.

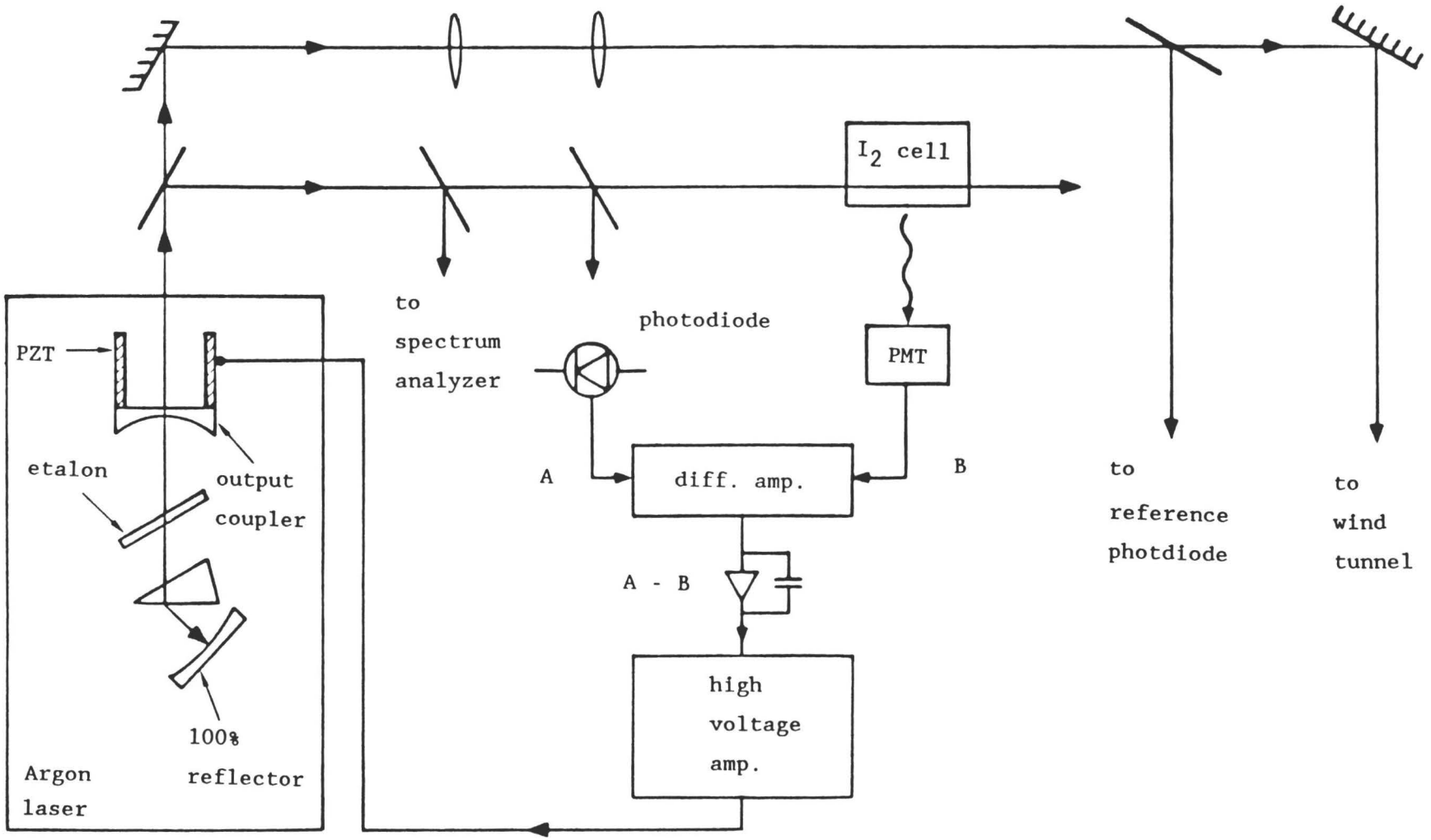

Figure 4.5 Details of Frequency Stabilization for the Argon-Ion Laser.

The degree of the long term frequency stability of the argon-ion laser can be estimated as follows. A rough estimate of the slope of the I_2 lineshape at the half power point is the peak height divided by the full width at half maximum (FWHM), which is about 1000 MHz for the I_2 line. As the error voltage randomly fluctuates near its zero value, the laser will correspondingly fluctuate in frequency. The peak fluorescence voltage was typically 1700 mv, while the fluctuations of the error signal (before amplification) about zero were observed to be ± 5 mV while the laser was locked. Thus the long term (few seconds to a few hours) peak-to-peak frequency fluctuations are about ± 3 MHz (~ 2 MHz RMS).

The amplitude fluctuations of the probe laser are very important to an IRS experiment because the IRS signal is detected on top of the probe laser intensity. Random amplitude noise integrated over all frequencies was generally measured to be several percent of the total laser output. This noise may overwhelm the signal if not eliminated and will be discussed in more detail in Chapter V with the experimental results.

Since the pump laser is pulsed at 10 Hz, there is no need to have the argon-ion probe laser constantly illuminating the detection diode. Therefore the probe laser is chopped at 10 Hz with a mechanical chopper which is locked to the dye laser amplifier chopper such that the 5 nsec pump laser pulse occurs in the middle of the probe laser pulse. Probe laser pulses were made as short as possible without losing the lock between the two choppers. The difficulty of locking the two choppers varied from day to day, and so the width of the argon-ion probe laser pulses also varied from day to day. Some

days they were short as 100 μs and on other days they were as long as 700 μs. Chopping the probe laser this way reduces the average power incident on the diode, which allows higher probe laser power to be used without saturating the response of the diode.

4.5 Detection Electronics

The signal in an IRS experiment is an attenuation of the probe beam when a Raman resonance occurs. This attenuation is detected by monitoring the probe laser with a photodiode and is expected to be on the order of one percent of the total probe laser power for conditions typical of this experiment. The standard technique[32] for detecting a small (1%) and short (10 ns) absorption is to couple the detector to a fast amplifier (50 Ω input impedance) using a small capacitor (hundreds of pF). The capacitor and 50 Ω impedance act as a passive high pass filter which passes the 10 ns signal to the amplifier and blocks frequencies below 10 MHz. With this standard system, the intensity flucutations (0.1 $\rightarrow$ 10 MHz) of the probe laser were typically 20% of the Raman signals. To further reduce the probe laser intensity fluctuations, a differential detection scheme was used.

This detection scheme is shown in Figure 4.6. The intensity of the reference beam is carefully adjusted to equal the intensity in the signal beam. Thus the signal and reference diodes produce equal voltages. Since the two diodes are back-to-back, the currents through the 100 kΩ resistor are in opposite directions. Hence, any current fluctuations from the signal diode cancel with the fluctuation from the reference diode. The two identical photodiodes

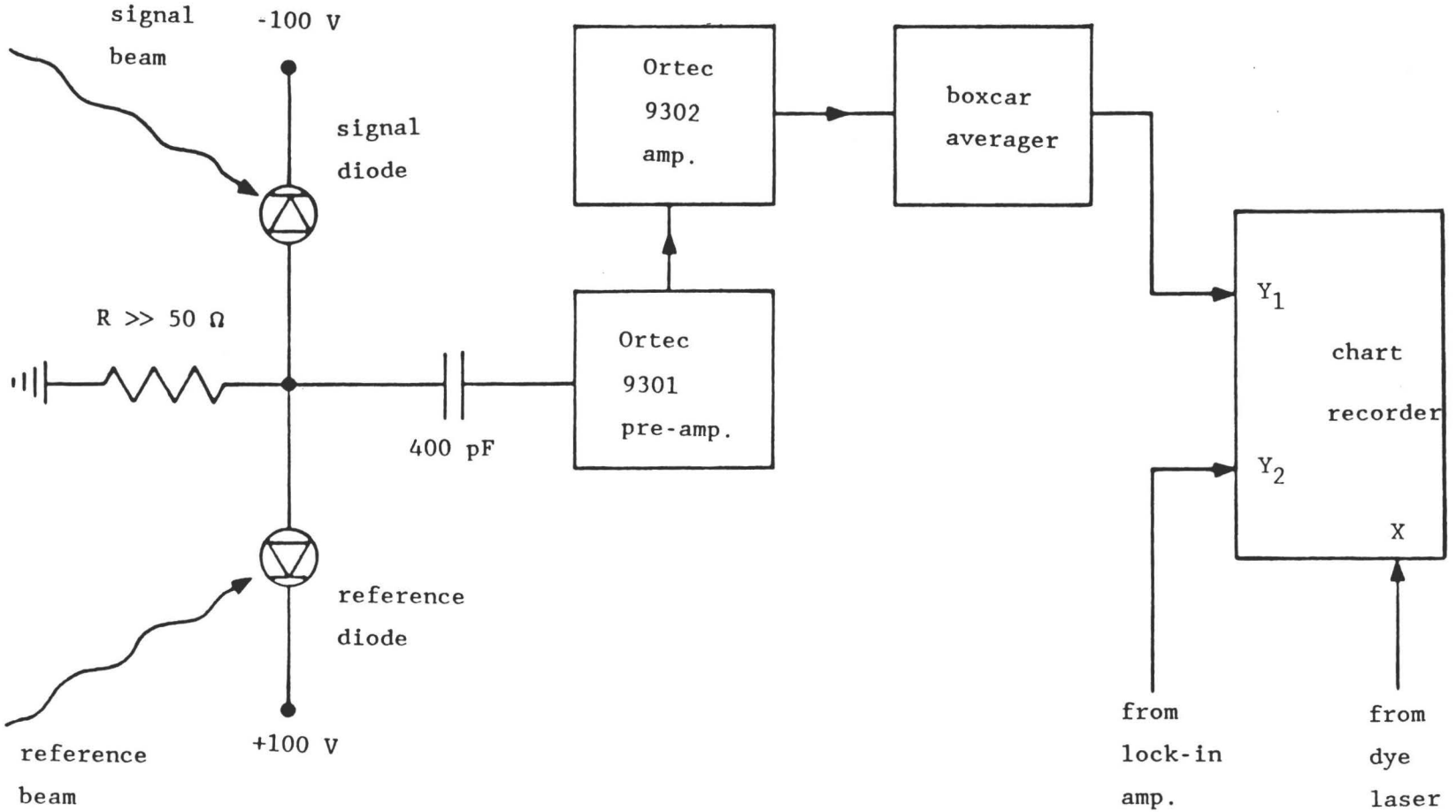

Figure 4.6 Detection Electronics for IRS Absorption Signal On the CW Argon-Ion Probe Beam.

are E.G. & G. FND-100 and are reverse biased with 100 volts. They have sensitivities on the order of 0.3 amps/Watt and risetimes of less than 1 nsec. A 400 pF capacitor blocks the 500 μs probe pulse, while allowing the 5 nsec signal to pass through to the pre-amp. The 50 Ω input load resistor of the pre-amp in combination with the 400 pF capacitor consititutes a passive high pass filter which helps reduce the amplitude fluctuation noise at frequencies below a few megahertz. The preamplifier and amplifier are Ortec models 9301 and 9302, respectively. The amplified pulse is then averaged with a P.A.R. model 162 boxcar averager which is simply used as a gated integrator with an adjustable averaging time. Effective time constants on the boxcar average varied from one to five seconds, depending on the frequency width of the scan and the width of the spectral features being observed. This averaged N_2 Raman spectrum is then recorded simultaneously with the Doppler-free hyperfine structure of an I_2 line on a dual pen chart recorder; the horizontal axis was driven with a voltage that was proportional to the dye laser frequency.

As discussed in Chapter 2, a CSRS signal at 6767 Å is generated simultaneously with the IRS signal on the 5145 Å probe laser. This coherent signal beam, shown in Figure 4.1, may be detected simultaneously with the IRS signal. To eliminate stray light from the 6767 Å CSRS signal that exits the prism, the beam was passed through a Corning CS-259 colored glass filter and then through a Jarrel-Ash 0.5 m monochrometer. The detector was a ITT FW-130 photomultiplier biased at -1000 volts. The signal pulses from the photomultiplier

were amplified with Ortec amplifies (models 9301 and 9302) and averaged on a P.A.R. boxcar averager (model 162).

4.6 Wind Tunnel

The design of the supersonic wind tunnel used in the present measurement was based on three criteria:

1) Obtaining supersonic flow parameters (velocity, temperature, and density) which are similar to a full scale facility.

2) The limited pumping capability (mechanical pump) available in our laboratory.

3) Densities of 10^{18} cm^{-3} or greater are necessary for a good signal-to-noise ratio in the N_2 Raman spectra.

These conditions require that the supersonic flow region be restricted to 3 mm in diameter. The generation of a supersonic flow, as discussed in Chapter 3, requires a converging (cross sectional area decreasing along flow axis) channel followed by a diverging channel. Gas which has approximately zero velocity at the entrance to a convergent-divergent channel (also called a De Laval nozzle) is first accelerated to sonic velocity at the throat (minimum diameter) and then to supersonic velocities in the following diverging region. The roughness of the wind tunnel walls affects the amount of friction and non-isentropic flow. Thus, glass was used for the inside wall material to provide a

relatively smooth surface with a minimum amount of friction. The converging-diverging geometry was made by heating and stretching a short piece of 3 mm diameter commercial tubing. The end result was a 50 mm piece of tubing which was necked down to a minimum inside diameter of 1.8 mm. The general shape is shown in both Figures 4.1 and 4.7. On the input side, the 3 mm inside diameter was necked down to the 1.8 mm over a distance of a few millimeters. On the output side, where the supersonic flow was generated, the inside diameter was smoothly increased back to 3 mm over a distance of about 20 mm. This was followed by a 25 mm test section where the inside diameter was roughly constant at 3 mm. At both ends the outside diameter was about 5 mm.

A detailed sketch of the entire wind tunnel assembly is shown in Figure 4.7. Two separate cavities (one on the input side and one on the output side of the flow region) were carved out of a solid aluminum block. The input cavity volume was about 30 cm^3, while the output cavity was closer to 50 cm^3 in volume. The two cavities were connected by the 5 cm long glass tube described above. Both cavities had windows (tilted at Brewster's angle) which allowed the overlapping and copropagating laser beams to enter the window on the output cavity, travel down the axis of the glass tube, and exit through the window on the input cavity. Nitrogen was supplied to the input cavity from a commercial high pressure bottle, while a 300 liter/min pump carried the nitrogen out through the outlet cavity. A mercury manometer was used to monitor the pressure in each cavity. When the input cavity was

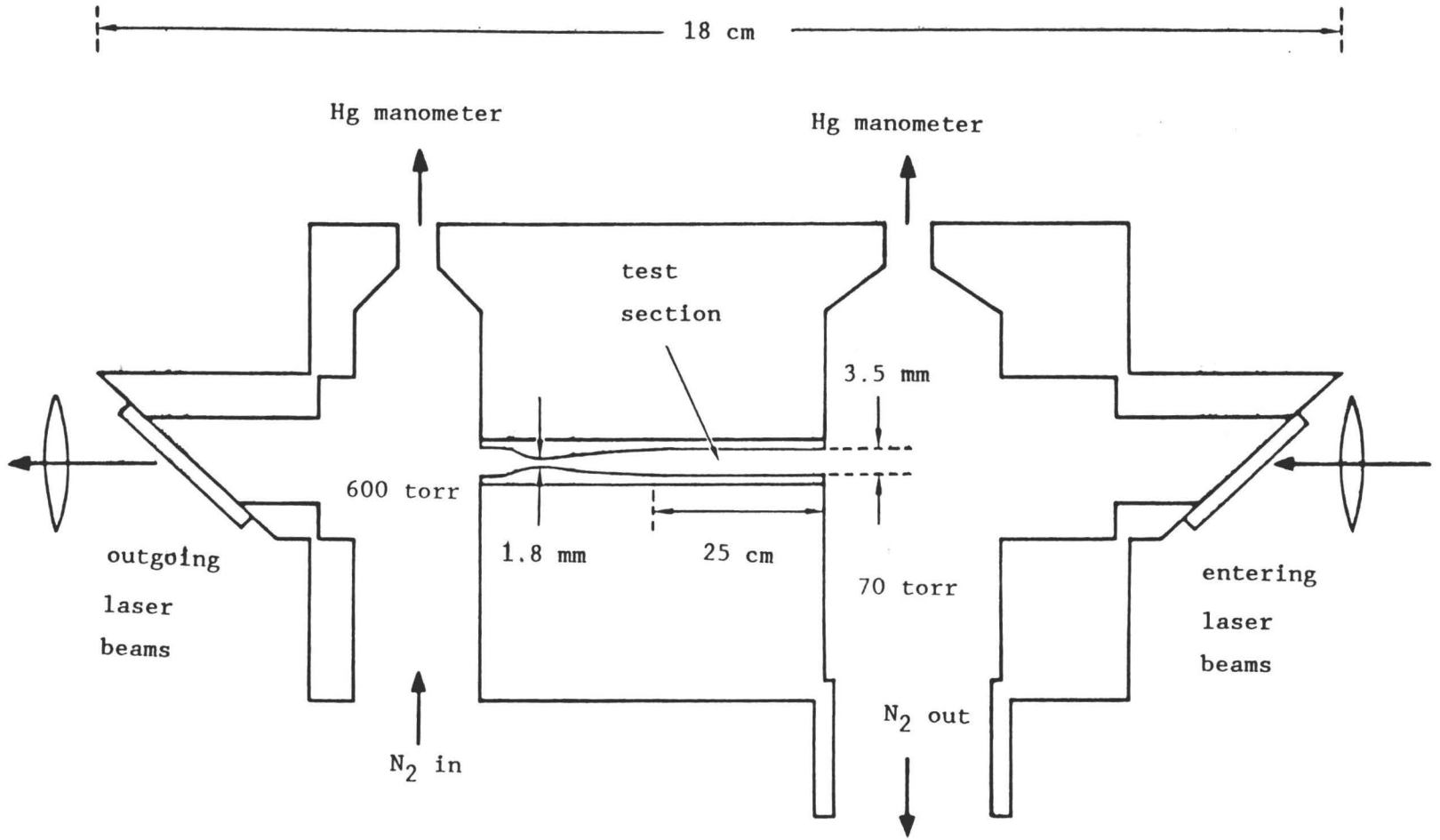

Figure 4.7 Full Scale Drawing of the Miniature Supersonic Wind Tunnel Used to Generate the Mach 2 Flow.

maintained at about 600 torr, the pressure in the exit cavity was typically set at 70 torr.

These conditions generated an approximately isentropic supersonic flow in the expanding region of the glass tube. The flow parameters remained approximately constant with axial position in the constant area portion (the test section) of the tube. The typical conditions in the test section are axial velocities of 500 m/s (Mach 2), temperatures of 150 K, and pressures of 40 torr. Because of a small amount of friction, the flow is not perfectly isentropic. In fact, the flow does slow down and simultaneously heat up as it traverses the test section (see Chapter 3.2). At the end of the tube a shock wave reduces the velocity and increases both pressure and temperature to match the conditions in the output cavity.

CHAPTER 5

Results and Discussion

This chapter presents the results of velocity, temperature, and density measurements using IRS in a supersonic flow. The uncertainties of the measurements and their sources will be discussed. Measurements using conventional techniques (e.g., pitot tube and thermocouple measurements) for comparison were not possible in the small flow volume used in this experiment. The intrusive nature of these probes would have disturbed the very flow parameters to be measured. In the absence of a better check, the supersonic flow parameters are calculated from isentropic and frictional flow models of Chapter 3 and compared to the present results. Reasonable agreement is found, considering the approximations used in the model. In addition to flow parameter measurements, the results of signal strength measurements for IRS and CSRS are presented and compared to signal sizes expected from the predictions of Chapter 2. Finally, measurements of pressure broadening coefficients for a few rotational transitions in the Raman Q branch of N_2 are presented and compared with previous work.

All the flow parameter measurements reported in this chapter were made in the 25 mm long constant area portion (test section) of the wind tunnel shown in Figure 4.7. There are small velocity,

temperature, and density gradients along the axis of the test section. Since the laser beams are focused to a minimum waist of ~ 30 μm in the test section, 75% of the coherent Raman signal is generated over a finite length of 1 cm, centered around the focal plane. Thus all of the flow parameter measurements are averages over the 60 μm diameter and approximately 1 cm long cylindrical region which is collinear with the axis of the flow tube and which is centered around the midpoint of the test section with an accuracy of ± 3 mm in length and ± 1 mm in radial position.

5.1 Velocity Measurements

The flow velocity was determined by measuring the frequency shift due to the Doppler effect of a Raman transition. An example of a single velocity measurement is shown in Figure 5.1. This figure shows two different scans over the same Raman vibrational Q branch (J = 8) transition in N_2. The solid curve was obtained under static conditions with 70 torr of N_2. The dotted curve shows the same transition obtained when supersonic flow was induced through the test section, by maintaining the entrance and exit chambers at 570 and 73 torr respectively. These two scans were recorded at different times (one right after the other), about 5 minutes apart, and were overlaid afterwards. The non-linearities of the cw dye laser scan (± 5%) are not repeatable from scan to scan and the absolute calibration of dye laser scan width is known to only 10% accuracy. Thus saturated absorption spectra of I_2 were simultaneously recorded with each of the Raman scans to calibrate the Raman Doppler shift. The saturated

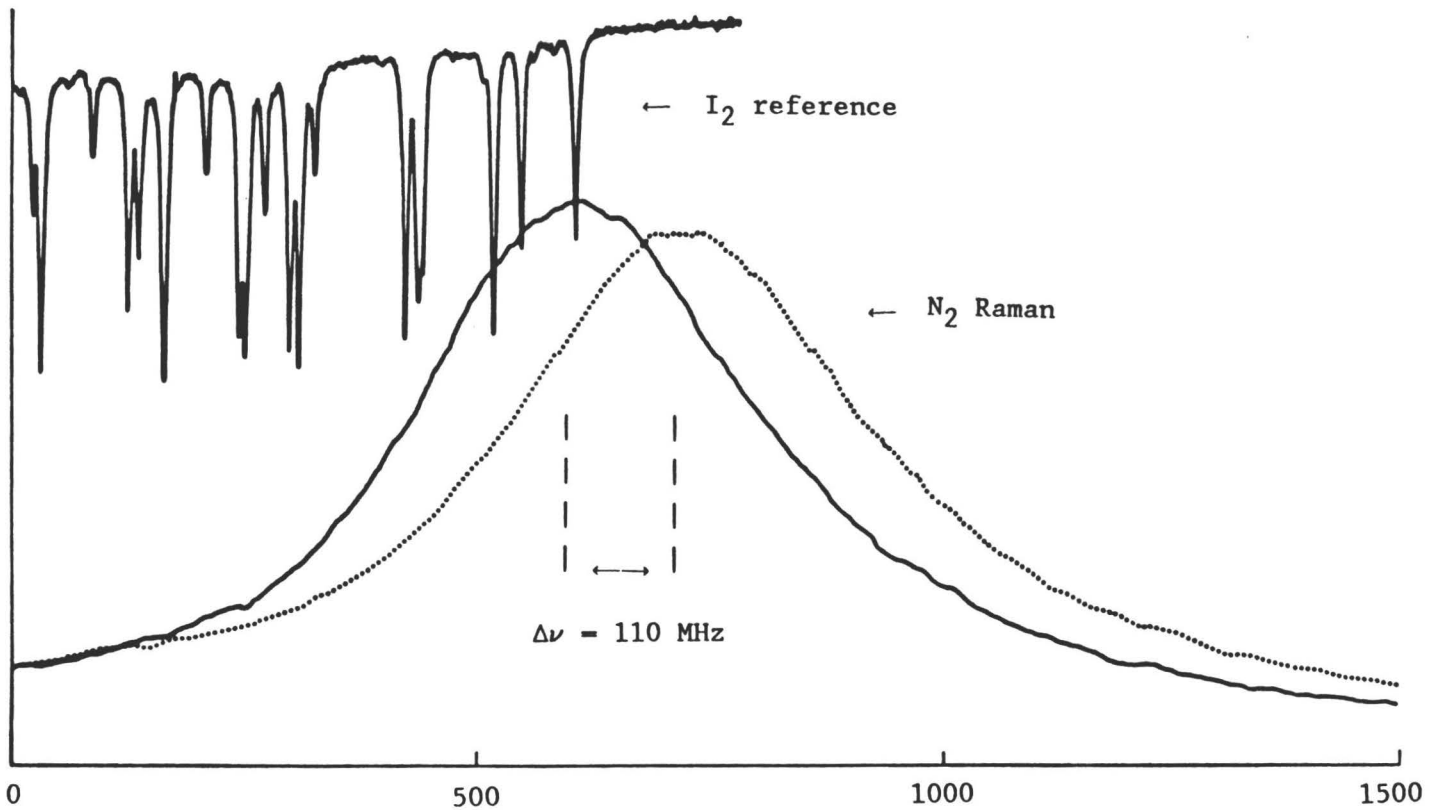

Figure 5.1 Doppler Shift of Q(8) Due to 475 m/s Supersonic Flow. The time constant is 5 s.

absorption spectrum is shown in the upper left hand corner of Figure 5.1. Since the I_2 peaks are unrelated to the N_2 flow in the test section, the two Raman scans are overlaid by superposing the I_2 peaks which lie nearest to the Raman peaks. Only the I_2 peak nearest the Raman peaks was used as a reference to minimize any uniform non-linearities in the dye laser scan. The magnitude of the frequency difference between the two Raman peaks was then referenced to the two I_2 peaks nearest the Raman peaks. After the simultaneous Raman and I_2 scans were completed, simultaneous scans of the I_2 peaks and the interferometer (75 MHz free spectral range) peaks were obtained, which allowed the separation of the I_2 peaks to be referenced to the calibrated interferometer. Without the interferometer reference, the laser scan width is only known to an accuracy of 5-10%. Therefore the Raman Doppler shift is ultimately referenced to the calibrated interferometer (see Chapter 4) instead of the laser scan width. Each of the two scans in Figure 5.1 was 5 minutes long with a time constant of 5 sec. Eq. (2.41) yields a velocity of 475 m/s for the 110 MHz frequency shift shown in Figure 5.1.

The best velocity measurement, shown in Table 5.1, was obtained with seven consecutive scans, alternating between flow and static conditions. Each scan was 5 min. long and the total measurement time was 45 min. Scans 2, 4, 5, 6 were flow runs made with entrance and exit chamber pressures of 570 ± 20 torr and 73 ± 3 torr, respectively, where the errors in the pressure readings represent the maximum variation over all the scans. Scans 1, 3, 7 are zero velocity reference scans under static

Table 5.1

Statistical Variations of Velocity Measurements
With Inverse Raman Spectroscopy

SCAN NUMBERS	SHIFT (MHz)	VELOCITY (m/s)
1,4	107	462
1,5	108	467
1,6	113	488
1,7	111	480
2,4	107	462
2,5	109	471
2,6	114	493
2,7	111	480
3,4	105	454
3,5	105	454
3,6	110	462
3,7	107	471
Average	109	471
Statistical Errors (1σ)	3	13
Systematic Errors	10	43

conditions at 70 torr. The 7 spectra yield the 12 data points listed in Table 5.1. Although these 12 measurements are not completely independent of each other, they shall be taken as independent for the present analysis. The 12 measurements give an average frequency shift of 109 ± 3 MHz. The statistical error given is one standard deviation.

Four sets of velocity measurements were made, where each set corresponds to the measurements made on a different day. These four data sets are illustrated in Figure 5.2. Sets 3 and 4 were preliminary runs that had significantly poorer signal-to-noise ratios. More importantly, sets 3 and 4 did not use the Doppler-free I_2 peaks and interferometer as a frequency reference; sets 3 and 4 used the dye laser scan width to calibrate the Doppler shift and used Doppler broadened (1 GHz FWHM) I_2 lines as a frequency reference. The error associated with this method is illustrated by sets 3a and 3b, which show measurements under the same flow conditions on the same day. Set 3a measurements were made with J = 8, and set 3b measurements were made with J = 10. Thus the only difference in the two sets was that the frequency of the dye laser was changed and a different Doppler broadened I_2 line was used as a frequency marker. Sets 1 and 2, however, used the I_2 hyperfine peaks (Figure 5.1) and the calibrated interferometer. Set 2 corresponds to the data of Table 5.1.

The accuracy in the best (Set 2) present measurements is limited by several systematic effects. First, the finite signal-to-noise ratio of the Raman spectra limit how accurately the center of each line can be determined. Second, typical

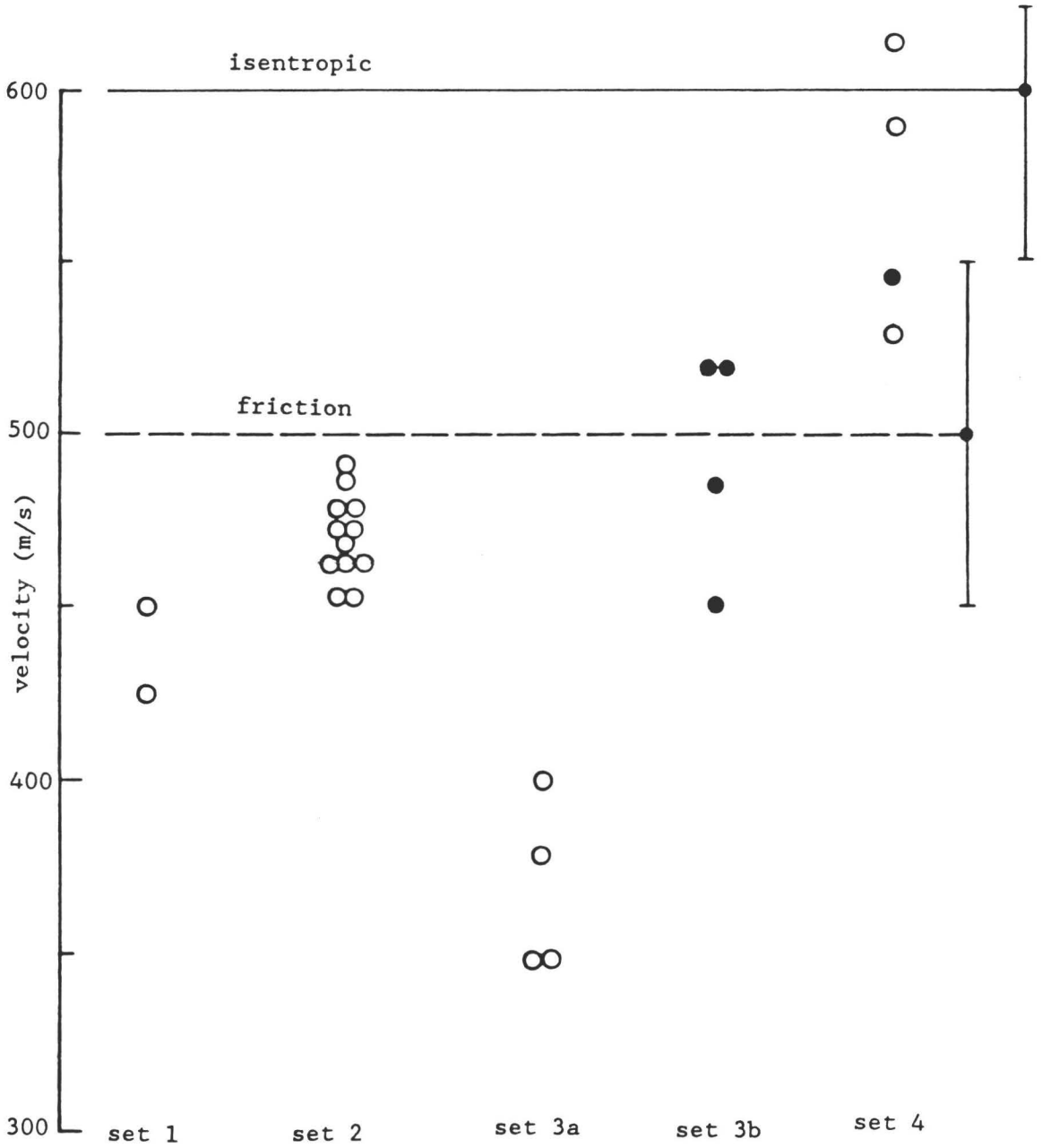

Figure 5.2 Comparison of Different Velocity Data Sets with Isentropic and Friction Flow Models. Solid dots are measurements using J = 10 and open dots are measurements using J = 8.

frequency shifts are 100 MHz, so errors of ± 5 MHz may be expected due to laser scan non-linearities. Third, the slow frequency drift of the stabilized single-mode argon-ion probe laser is estimated to be ± 3 MHz (see Section 4.2). Fourth, the high intensity of the pump beam is on the borderline of altering the lineshapes through the ac Stark effect. The magnitude of the Stark splitting (which causes an asymmetry as well as a broadening of these spectral lines) has been calculated by Huo[34] and is small for the intensities used in this work. A very small asymmetry in the lineshapes is usually observed even for no flow scans with short time constants. Since both the flow and no-flow lineshapes are recorded with identical laser intensities, the error introduced in the relative frequency shifts is expected to be small. Fifth, in the test section, a small velocity gradient exists over the measurement region. This gradient will alter the lineshape and introduce a systematic error in the relative frequency measurement. The velocity gradient was estimated to be about 20 m/s over the 1 cm measurement region, corresponding to a frequency spread of 5 MHz in the Doppler shift and an uncertainty of ± 2.5 MHz. Sixth, the flow and no flow scans were recorded at different pressures (≤ 30 torr difference), so pressure shifts need to be considered. Pressure shifts are less than .001 cm^{-1}/atm[35] and contribute a maximum possible systematic error of 1 MHz. The final systematic error considered is the frequency shift that has been observed between the cw input and the pulsed output of the pump laser. Wieman[36] has observed in his pulsed amplifier that this shift is alignment dependent and constant

throughout a single day if the alignment is not altered. In this work, the amplifier alignment was not adjusted between flow and no-flow scans and hence systematic errors of this origin are expected to be small. The total systematic error is estimated by adding the individual components and is about 10 MHz for these measurements.

The present measurements are then limited by several effects, and some may be reduced. The frequency stability of the argon-ion probe laser may be improved by temperature stabilizing the I_2 cell which is used for the frequency locking. Alternatively, the argon-ion laser could be locked to a narrow (10 MHz) hyperfine I_2 component, obtained with saturation spectroscopy, rather than to the broad (1000 MHz) Doppler broadened transition used here. Additionally, if the flow and no flow measurements are made simultaneously, one might cautiously expect that these systematic errors could be reduced to one MHz.

The S/N of the Raman spectra are ultimately limited by the shot noise of the argon-ion probe laser intensity which is incident on the detector. The present measurements are estimated to be about one order of magnitude above the shot noise limit. Most of this noise is attributed to fluctuations in the intensities of the two lasers. A division scheme (where the signal magnitude is divided by one or both laser intensities for each pulse rather than subtracting) would improve the S/N of the Raman spectra of the present work. Only a single channel boxcar was available for the present measurements and thus normalizing to the laser powers was not possible. In addition, the differential

subtraction scheme is not perfect (possibly because the two diodes did not have the exact same risetimes), so there is residual noise from the flucuations of the probe laser intensity which is incident on the detector. This noise source could be avoided altogether if CSRS, rather than IRS, were used. Unlike the IRS detector, the CSRS detector does not have the probe beam incident on it. Electronic noise, e.g., noise on the amplifier, RF pick-up from the pulsed YAG, and possibly noise originating inside the box car averager, was also observed. Any large reduction in laser intensity fluctuations would make electronic noise the dominant noise source. These electronic noises would then have to be dealt with in order to approach the shot noise limit. The above mentioned improvements provide the possibility for a substantial reduction of the errors reported in these velocity measurements.

5.2 Temperature and Density Measurements

Temperature Measurements

The rotational temperature of the supersonic flow is obtained by measuring the relative strengths of two rotational Raman transitions and calculating the temperature from the Boltzman distribution. In this measurement, the peak heights of each transition are taken as the relative strengths, since the linewidths and lineshapes of adjacent J transitions are observed to be the same. The transit time for a molecule down the test section is 50 μs, while the mean time between molecular collisions is about 10 nsec for the test section flow conditions. Because of the fast collision rate and fast rotational relaxation time,[37] the

translational temperature will be equal to the rotational temperature for these measurements. Hence the two temperatures shall no longer be distinguished, and all the measurements reported in this section are both rotational and translational temperatures.

Two different temperature measurements, corresponding to the upper and lower spectra, are shown in Figure 5.3. Both of these scans are over the transitions J = 8, 9, and 10 in the Q-branch of the v = 0 to v = 1 vibration transition in N_2. The upper curve was recorded under no flow conditions at 73 torr and room temperature. The lower curve was recorded under the same supersonic flow conditions as the velocity measurement shown in Figure 5.1. The time constant for both traces was 2 sec while each scan lasted 10 min. Using the relative heights of J = 8 and 10 in Eq. (2.44) yields temperatures of 314 K for the top spectrum and 181 K for the bottom spectrum.

The best temperature data set, taken on the same day as the velocity data set from Table 5.1, is shown in the top half of Table 5.2. This set consisted of three successive 10 min. scans over a period of 35 min, for the same entrance (P_o = 570 torr) and exit (P_b = 73 torr) pressures used in the velocity measurement. Since the optical alignment was not changed between the velocity and temperature measurements, the measurement volume is the same for both measurements. Each row in Table 5.2 contains the temperature measurement determined from a different pair of J transitions. Note that the variations from scan to scan for J = 8 and 10 are smaller than for many other J combinations. The reason

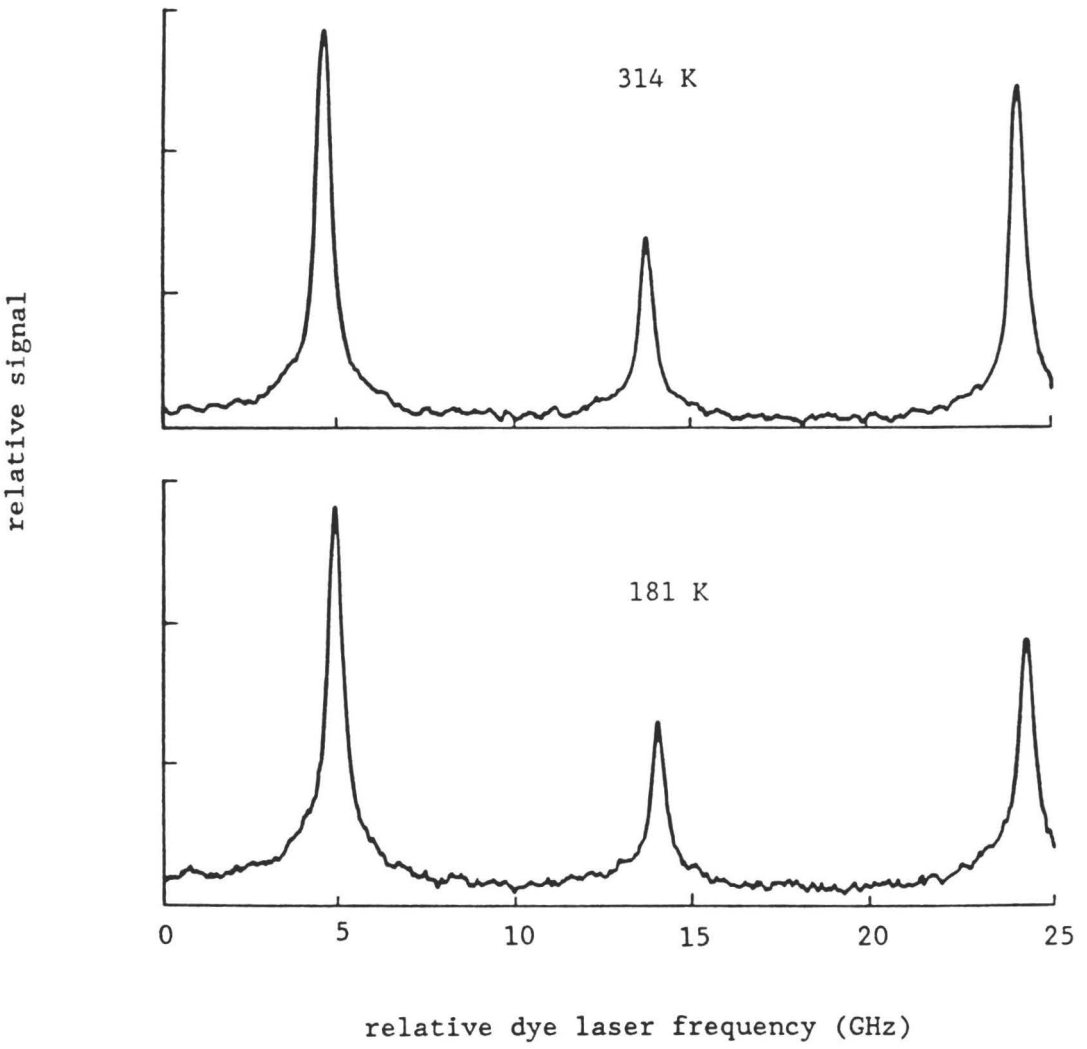

Figure 5.3 Raman Scans Over Q(8), Q(9), and Q(10) in N_2 for Temperatures of 314 K and 181 K. The time constant is 1 s.

Table 5.2

Temperature (K) Measurements from Various Combinations of Transition Pairs in the Q-Branch

Supersonic Flow Temperature

J Levels Used	Scan 1	Scan 2	Scan 3
7, 8	162 (25)	175 (30)	160 (25)
7, 9	152 (20)	189 (30)	176 (25)
7, 10	171 (10)	181 (10)	170 (10)
8, 9	144 (25)	204 (40)	191 (35)
8, 10	175 (10)	181 (10)	175 (10)
9, 10	218 (50)	167 (30)	162 (30)

Weighted Average = 174 ± 4 K

Static Room Temperature Sample

J Levels Used	Scan 4	Scan 5	Scan 6
7, 8	285 (100)	396 (140)	396 (140)
7, 9	289 (60)	334 (80)	324 (70)
7, 10	284 (30)	331 (35)	342 (40)
8, 9	291 (90)	264 (80)	277 (80)
8, 10	286 (30)	314 (30)	322 (30)
9, 10	276 (80)	366 (100)	380 (120)

Weighted Average = 307 ± 8 K
Hg thermometer = 298 K

for this is because the even numbered J transitions are twice as strong as the odd numbered transitions due to nuclear spin degeneracies. Stronger transitions are expected to give more accurate temperature measurements because of their larger S/N. The error for each individual measurement, shown in parenthesis in Table 5.2, was determined in the following manner. The fractional uncertainty in the line strengths was estimated as the ratio of the noise to peak height. The fractional change in temperature was related to fractional change in transition strength by differentiating Eq. (2.44), and then the fractional error in the temperature measurement was calculated.

The reciprocal of the square of these individual errors were then used as the weights to calcuate a weighted average of the whole set. This weighted average for the data in the top half of Table 5.2 is 174 ± 4 K, where the error of ± 4 K is one standard deviation of the weighted mean. For comparison, a temperature measurement made on a sample at room temperatures (no-flow condition) is shown in the lower half of Table 5.2. The room temperature was simultaneously measured to be 298 K with a Hg thermometer.

Four different flow temperature data sets are shown in Figure 5.4. Each set corresponds to a different day (and possibly different radial position in the flow tube). Data set 1 in Figure 5.4 corresponds to the same day as data set 1 in Figure 5.2, etc. To keep the figure uncluttered, only the most accurate measurements (from J = 8 and 10 or J = 10 and 12) from each data set are shown.

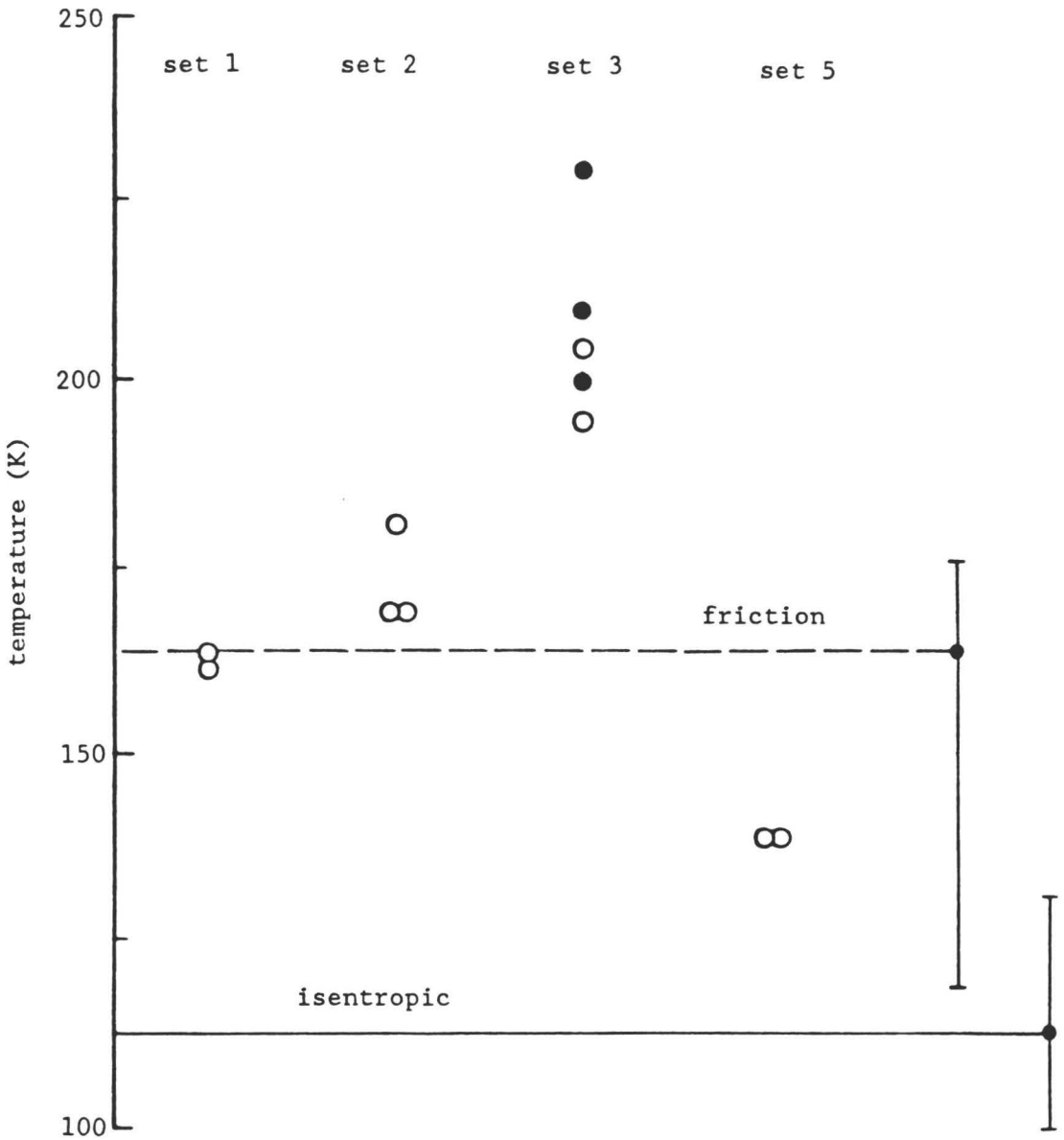

Figure 5.4 Comparison of Four Temperature Data Sets with Insentropic and Friction Flow Model Predictions. Solid dots use J = 10 and 12, while open dots use J = 8 and 10 for the temperature measurement.

The systematic errors associated with this temperature measurement are less severe than those discussed earlier for the velocity measurement. The relative strength of two Raman transitions is determined solely from the peak heights. This assumes the linewidth and lineshapes of adjacent J transitions are identical. This is a good assumption since the difference in self pressure broadening coefficients for adjacent J transitions is .001 cm^{-1}/atm.[38] This corresponds to a 2 MHz difference in the linewidths of two adjacent J levels at 50 torr, while the linewidths are 500 MHz. The difference in lineshapes due to Stark broadening also should be considered. For the intensities (30 GW/cm^2) used here, the difference (due to different Stark splitting) in linewidths of J = 8 and 10 is estimated to be about 2 MHz.[39] For Stark splitting as small as this, the difference in the asymmetry of the two lines can also be neglected. Finally the Doppler broadening difference between two adjacent transitions is completely negligible. Thus, the total contribution of these systematic errors to the temperature measurement is about 1%. In comparison, the statistical error for the measurement in Table 5.2 is 3%. Since the above errors are limited by the signal-to-noise of the Raman spectra, the same division scheme as suggested to improve the velocity measurements would also help improve the accuracy of these temperature measurements.

Density Measurements

The density of the supersonic flow was determined by comparing the relative transition strengths of one particular J

level for a flow and no-flow conditions, where the no-flow density was determined with a thermometer, a manometer and the ideal gas law. Because of different pressures and temperatures, the lineshapes for the flow and no flow conditions may differ from one another; thus relative transition strengths were determined by measuring the area under each line.

Areas were measured using a planimeter. For a given density, the fraction of molecules in state J is temperature dependent. Since the flow and no flow scans are made at different temperatures, the relative area measurement between flow and no flow scans needs to be corrected for the temperature difference in order to give the correct relative density.

The density measurement made from the same set of scans used in Table 5.2 is shown in Table 5.3. The numbers shown represent the total area under the curve for J = 8 as determined with the planimeter. Scans 1-3 are the same three flow scans listed in Table 5.2 for the temperature measurement. Scans 4-6 are no-flow runs; 4 and 5 were taken before the flow runs, while 6 was taken afterwards. Each scan was 10 min long, so the set of six scans represents an averaging time of 60 min. For each scan, the area of J = 8 was traced 3 times; the averages for the nine flow and the nine no-flow traces are shown in the right hand column of Table 5.3. The temperature measurement, from Table 5.2, can be used to calculate the ratio of population of J = 8 at 175 K and 298 K, which is 0.971. This correction along with the two averages in Table 5.3 yields a relative density of flow to no-flow of 0.97. The no flow runs were made at 71 ± 2 torr and 298 K,

Table 5.3

Density Measurements for the Same Scans Listed in Table 5.2. The numbers show the total areas (in arbitrary units) of J = 8 for successive planimeter traces.

		PLANIMETER TRACE			AVERAGE
		1	2	3	
FLOW SCANS	1	223	224	225	223 ± 4
	2	225	227	228	
	3	219	218	216	
NO FLOW SCANS	4	223	218	220	224 ± 4
	5	225	227	227	
	6	222	226	231	

thus the flow density (for the temperature measurement in Table 5.2) is 2.2 x 10^{18} cm^{-3}. A similar analysis for the transitions J = 9 and J = 10 gave densities which were, respectively, 2% and 9% greater than the result for J = 8.

The error in the density measurement for J = 8 is estimated in the following manner. The statistical error in determining the ratio of the areas for the flow and no-flow transitions is 4%. The error in the correction factor of .97 is 4% due to the uncertainty the measured flow temperature. Summing these two errors gives a total error of ± 8% for the relative density measurement, which is consistent with the 9% difference between the J = 8 and the J = 10 measurements. Lastly, the error in the reference density is 3% due to uncertainty in the manometer reading. Thus the total uncertainty of the absolute density measurement is 11%.

Close examination of Figure 5.3 reveals a slight tilt to the baseline. This tilt is due to the non-symetric spacing of the different J components and will not appreciably add to the 10% accuracy of the present measurement. The baselines for the integrations of Table 5.3 were determined from the average position of the noise from both sides of the resonance. However, future reductions of the uncertainties to the 1% range will require an accounting for this baseline tilt.

The pressure for each data set can be determined from the measured density and temperature using the ideal gas law. Figure 5.5 shows the pressure for three data sets, where the set numbers correspond to those in Figures 5.2 and 5.4. The experimental

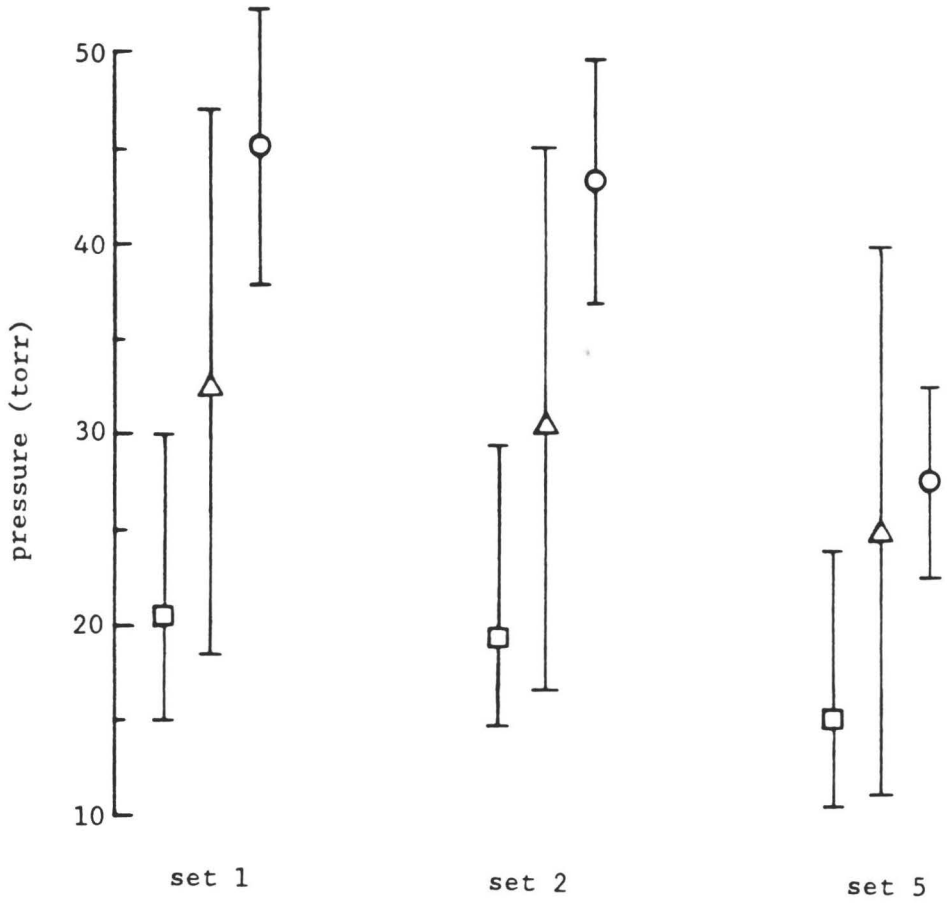

Figure 5.5 Comparison of Experimentally Determined Pressures [○] to Isentropic [□] and Friction [△] Flow Models.

pressure is obtained using average temperature and density for each set.

5.3 Comparison of Flow Measurements with One-Dimensional Flow Models

In this Section the results of velocity and temperature measurements in the supersonic flow are compared to a one-dimensional flow model. The major results of this model are summarized in Chapter 3. In addition to the one-dimensional simplification, the magnitude of the viscous interaction with the walls (i.e. friction coefficient f) is not well known. These two drawbacks mean that the model discussed here can only be used as a rough guide for the expected flow parameters. Thus the discussion in this section is not intended as a detailed study of the flow characteristics of the particular nozzle used in this experiment.

In Figure 5.2 the results of five different sets of velocity measurements are presented, where each data point represents a single measurement. Consider only data sets 1 and 2, since sets 3a, 3b, and 4 have considerable errors (± 25%) from reading the Doppler shifts directly from the dye laser scan width (see section 5.1). The solid horizontal line shows the frictionless insentropic velocity calculated from the results of section 3.1, while the dotted line shows the velocity expected when frictional effects are included by using the results of section 3.2. The uncertainty ($^{+20}_{-30}$ m/s) in the theoretical frictionless value is due to uncertainties of the nozzle dimensions, while the uncertainty (± 40 m/s) in the friction value also includes the uncertainty in the measured friction coefficient f. The value[40,41] of f used here is 0.03. Data sets 1 and 2 are in agreement

with each and are in reasonable agreement with the friction flow model.

There is another possible source of error in the viscous flow model. Recall, in Chapter 3, that radial distributions of the flow parameters were neglected. The radial velocity and temperature gradients are strongly dependent on several conditions: the magnitude of the viscous effect, the exact shape of the converging-diverging contour, whether or not the boundary layer is laminar or turbulent, and the Reynolds number. Since these conditions can only be approximated for the nozzle used here, the radial gradients cannot be accurately calculated. However, it has been demonstrated[42] that friction effects in a supersonic pipe flow can be approximated by supersonic flow near a flat plate. Thus, an order of magnitude estimate can be made by considering laminar supersonic flow over a smooth flat plate.[43] The result of this type of estimate yields a difference of 10% between the velocity on the centerline and the velocity 1 mm off the centerline of the nozzle. Thus flow gradients inside the tube could explain the magnitude of the day-to-day variations of the different velocity sets of Figure 5.2 if the measurements of each day are assumed to be made at randomly different radial positions inside the flow tube. However the 25% uncertainties of most of the data sets in Figure 5.2 prohibit the conclusion that these variations must be due to radial flow gradients.

In Figure 5.4 the results of four different sets of temperature measurements are presented. The perfectly isentropic prediction is shown with a solid horizontal line, while friction effects are included in the value indicated by the dotted line. The estimated

error in the frictionless value is $^{+20}_{-10}$ K, while the error in the friction value is ± 20 K. Considering the errors estimated for the one-dimensional flow model, the results of most of the measurements are in general agreement with the model. However, the results of the different sets are in slight disagreement with one another. The most plausible explanation for the differences between different sets and for the difference between the measurements and the model is the one-dimensional aspect of the model. While the one-dimensional model assumes constant temperatures over the circular cross section at a given point in the test section, a more realistic model would include temperature gradients which are transverse to the direction of the flow. The radial position of the measurement for each velocity set was not well known (± 1 mm), and was certainly different for most measurement sets. An order of magnitude estimate[43] of the temperature gradients in the radial direction suggests that temperatures could be higher by 10% at 1.0 mm off the centerline. Thus radial gradients are estimated to be large enough to explain the difference in the results of different temperature data sets.

Finally, the average pressures (determined from temperature and density measurements) are compared with the isentropic (solid line) and friction (dotted line) models in Figure 5.5. The experimentally determined pressures agree with the friction flow model to within the combined uncertainties. The reasonable agreement of the measured velocity, temperature, and pressure with the flow model indicates that the IRS technique certainly has the potential to become a useful tool for probing supersonic flows. However, the crude nature of the model

used to describe the present flow prevents a close comparison (a few percent or better) of these measurements with a known flow condition.

5.4 Raman Signal Strength Measurements

IRS and CSRS spectra can be obtained simultaneously with the same experimental apparatus. Future improvements (see Chapter 6) in the present velocity measurements may require using the CSRS signal rather than the IRS signal, as as discussed in section 5.1. Thus it is useful to compare the signal-to-noise ratio of the two techniques. In addition it is interesting to compare the absolute signal strengths to those predicted by the theoretical results of Chapter 2. In this section a comparison of the relative S/N of IRS and CSRS will be presented first, followed by the results of absolute signal strengths measurements for both IRS and CSRS.

Raman scans over J = 7 and 8 are shown in Figure 5.6 for both IRS and CSRS for the same density at which the flow measurements in sections 5.1 and 5.2 were made. The two traces in Figure 5.6 show that the signal-to-noise ratio of the CSRS spectrum is about a factor of two better than the IRS spectrum. The small bump near the J = 7 transition in the IRS spectrum is noise (it is not repeatable). These signals were not normalized to the pump laser power. One expects that any improvements due to normalization would be more noticable on the CSRS spectrum, since the CSRS signal is proportional to the square of the pump laser power while the IRS signal is linearly proportional to the pump power. Thus, the sensitivities at this density for flow parameter measurements with CSRS can be expected to be the same as or better than those for the IRS measurements presented earlier. This

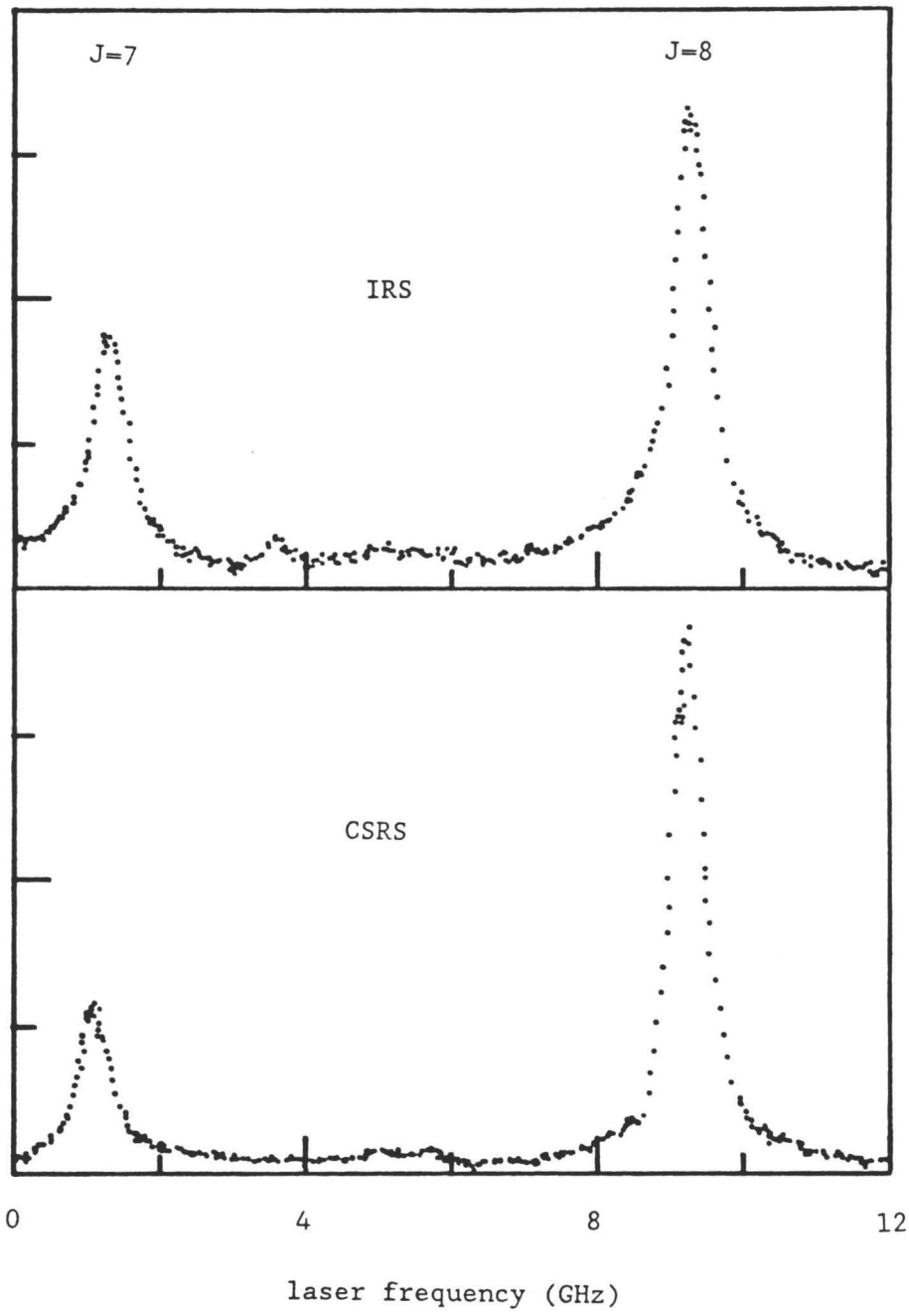

Figure 5.6 Signal-To-Noise Comparision Between IRS and CSRS. Experimental conditions are 295 K, 83 torr, 1 MW peak power in the 5 ns pump laser pulses, and 200 mW of probe power.

figure also illustrates the difference in density dependences in IRS and CSRS. The ratio of the line strengths for an even J line to an odd J line is 2:1 for IRS and 4:1 for CSRS. This is a result of a linear density dependence for IRS (see Eq. 2.36), a quadratic density dependence for CSRS (see Eq. 2.38), and a nuclear spin degeneracy which allows the even J lines twice the population density as the odd J lines. Because of the different density dependences, IRS can be expected to be better at lower densities, while CSRS should be better for higher densities.

The two spectra of Figure 5.6 were not acquired simultaneously because two identical detection channels were not available. The IRS scan was recorded immediately after the CSRS scan. Since each scan was ten minutes long (time constant = 1 s), the IRS and CSRS measurements are separated by ten minutes. Both the probe and pump laser powers were measured before, in between and after the two scans, to verify that the laser powers remained constant over both scans. In the interaction region, the probe power was 190 mW, while the peak pump power was 1.3 MW. The pressure and temperature were 83 torr and 295 K. Both the IRS signal (from the photodiode) and the CSRS signal (from the photomultiplier tube) were amplified and averaged with the same detection system.

Table 5.4 contains the results of three separate measurements of the measured signal strengths for both IRS and CSRS. The numbers in parentheses indicate the estimated error for each measurement or calculation. Each day's result is considered to be a separate measurement since the optical alignment changed from day-to-day. The result for 11/4/83 was obtained from the date of Figure 5.6, while the

Table 5.4

Comparison Between Theoretical and Experimental Raman Signal Strengths

		IRS (μW)		CSRS (μW)	
Date	Q(J)	Theory (Eq. 2.36)	Expt.	Theory (Eq. 2.38)	Expt.
12/10/82	8	2400 (240)	2400 (700)	13 (2)	19 (10)
12/31/82	6	3500 (350)	7400 (2200)	16 (3)	40 (25)
11/4/83	8	4600 (460)	3700 (1100)	23 (3)	3.4 (2)

results of 12/10/82 and 12/31/82 were obtained using room air (630 torr total pressure) as the sample. The calculated results are obtained from Eqs. (2.36) and (2.38), using the measured pump and probe laser powers, along with the previously[44] measured spontaneous Raman differential cross section of 4.3×10^{-3} cm^2/sr.

There are several sources of error in the comparison of Table 5.4. The error in the theoretical value is dominated by the uncertainty in the laser powers, which are 5% for each laser. The laser powers were measured with a Coherent (model 210) meter, which was later calibrated with a Scientech (Model 380101), absorbing power meter. The uncertainties in the IRS and CSRS calculations are 10% and 15% respectively.

Uncertainties in the experimentally determined signal strengths are due to the errors in measuring the various parameters (detector sensitivities, amplifier gains, etc.) in the detection system. The errors in the photomultiplier tube sensitivity, boxcar sensitivity, and amplifier gain are all estimated to be 10%. There is an additional uncertainty in the CSRS measurement since the photomultiplier tube was not fast enough to accurately reproduce the time profile of the CSRS signal. The CSRS time width was approximated in the following manner. The pump laser pulse was measured to be 5 ns, and was assumed to be a smooth Gaussian in shape for this analysis. In reality, the pump laser pulse is very spiky, where the spikes are too fast to be resolved on our detector. Since the CSRS signal depends on the square of the pump laser intensity, the CSRS width is expected to be the width of the product of two 5 nsec Gaussian pulses, or 3.5 ns. The observed CSRS pulse width (35 ns) is then divided by

3.5 ns to obtain an attentuation factor of ten due to the slow response of the photomultiplier. The error in this attentuation factor is estimated to be 20%. Finally, errors in reading dc voltages from the oscilloscope and reading the signal sizes from the spectra are 5%. Using the errors quoted above, the total uncertainty in the IRS and CSRS measurements are 30% and 60% respectively.

These calculations are made assuming both beams have TEM_{oo} modes and have the same waist size in the focal plane. Although the probe (Ar-ion) beam is close to an ideal TEM_{oo} mode, the pump beam is more of a filled in donut-mode because of the donut-mode YAG beam used to pump the final stage of the pulsed dye amplifier. The deviation of the pump beam profile from a TEM_{oo} mode is sure to produce differences in the calculated and measured beams. For simplicity, this effect is omitted from this analysis, however the reader should keep in mind that the error due to this approximation is probably more important than all of the errors mentioned above.

The errors described above can account for the differences between theory and experiment for four of the six comparisons in Table 5.4, but not for the discrepancies of the CSRS measurement on 11/4/83 and the IRS measurement on 12/31/82. The general agreement, however, of the measurements (except CSRS on 11/4/83) and theory shows that the classical model of Chapter 2 is accurate enough to predict the expected coherent Raman signals to within a factor of 3, despite the questionable approximations used in approximately the time and spatial profile of the pump beam.

One possible explanation for the large discrepancy of the CSRS results on 11/4/83 is a faulty photomultiplier tube. Although no

irregular behavior was noticed up to and including 11/4/83, the photomultiplier tube behaved erratically (the signal would slowly fade away over ~ 15 min and temporarily turning off the high voltage would cause the signal to reappear before fading away again) four days later. The cause of this behavior was never determined and the photomultiplier tube checked out normal (with a reasonable sensitivity and time response) a few days later.

5.5 Pressure Broadening Measurements

When the present flow measurements were made there was no published measurement of the pressure broadening coefficients for the vibrational Q-branch transitions in N_2. Since the temperature measurements of section 5.2 assumed that the broadening coefficient did not change significantly for two adjacent transitions, it was necessary to confirm this assumption with a measurement. Soon after the present pressure broadening coefficient measurements were made, Reference 35 was published. The Raman linewidths for three separate J transitions (J = 8, 9, 10) in the N_2 Q-branch ($v = 0 \rightarrow 1$) were measured using the flow chamber as a static cell. The measurements were made over the pressure range of 20 to 300 torr, where the pressures were read to $\pm$ 2 torr from a Hg manometer. The total integration time over a single line was varied from 20 sec for the 20 torr data points to 60 sec for the 300 torr data points.

The results for J = 8, 9, and 10, are shown in Figures 5.7 through 5.9 respectively, which illustrate both the data and best fit straight line. These three figures show the total observed linewidth as a function of pressure. A more exact analysis requires determining

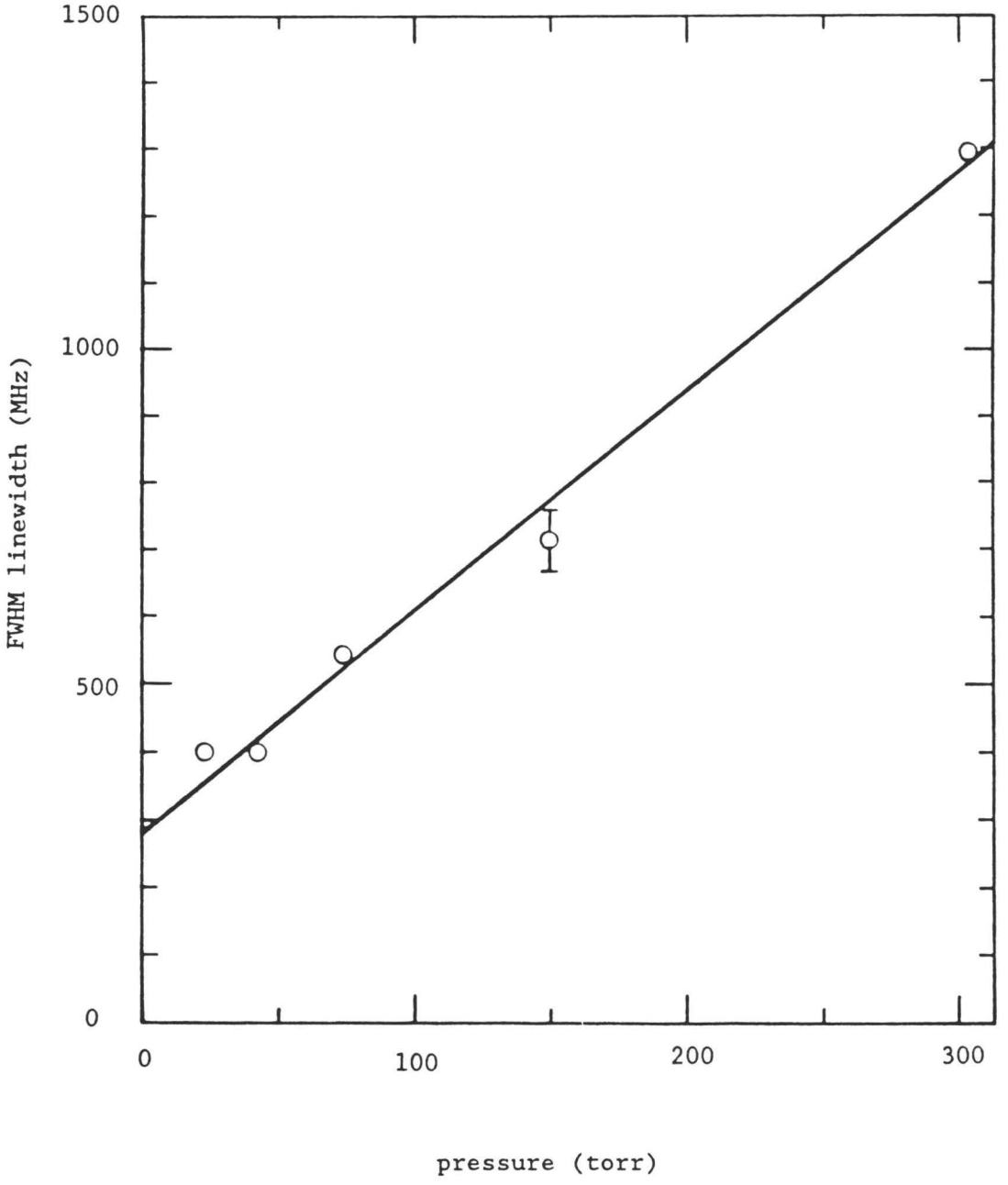

Figure 5.7 Raman (J = 8) Linewidth Versus Pressure.

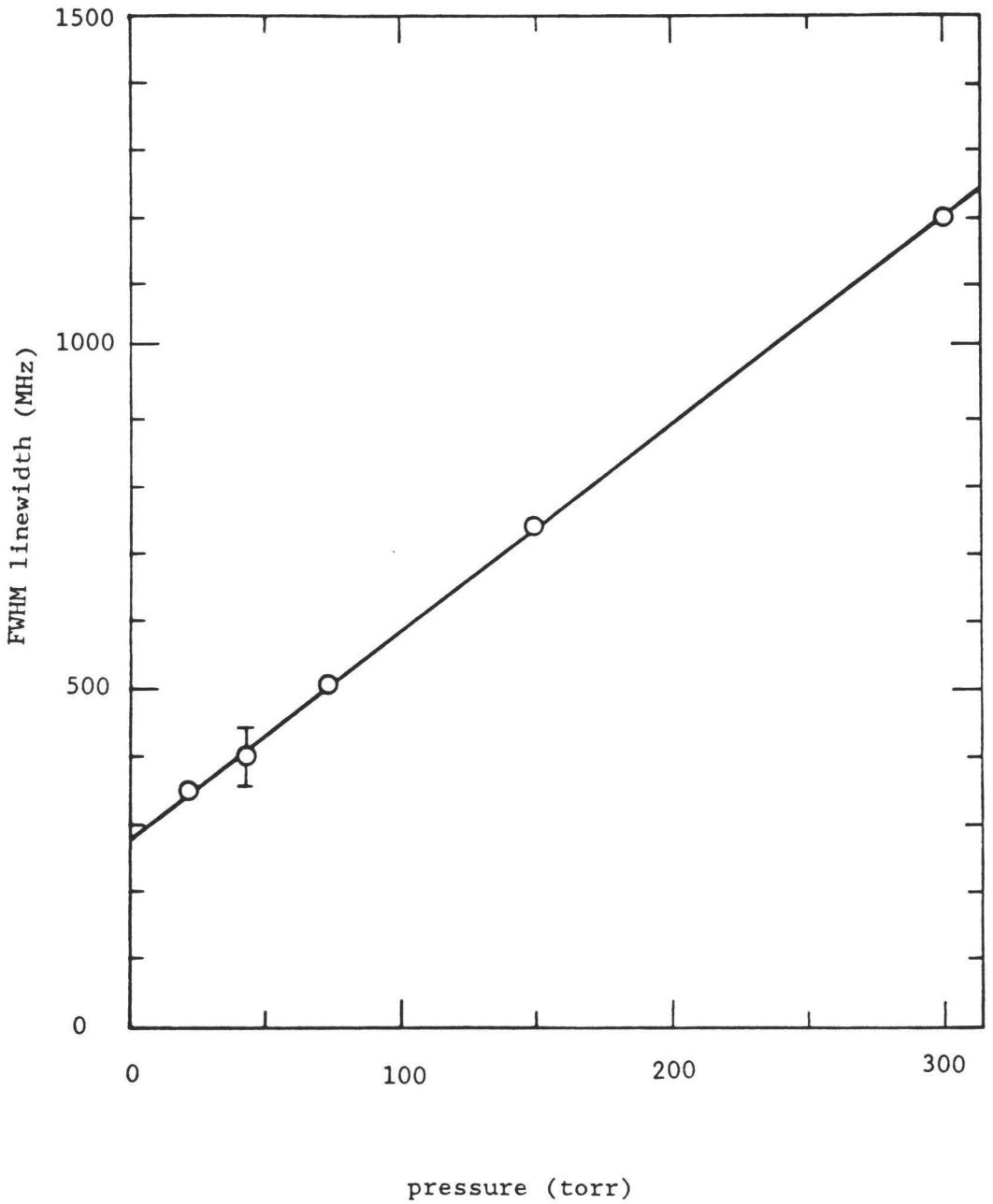

Figure 5.8 Raman (J = 9) Linewidth Versus Pressure.

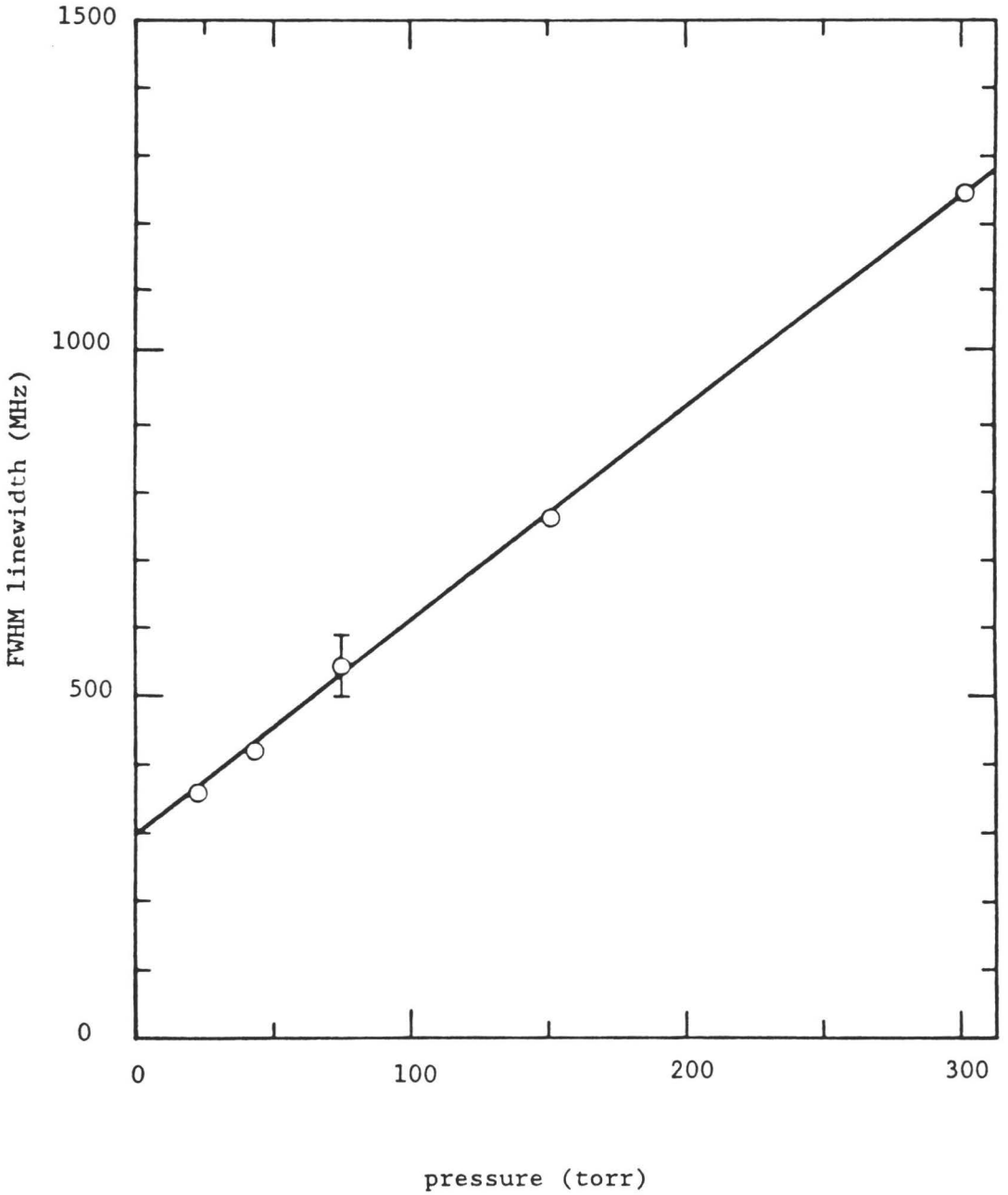

Figure 5.9 Raman (J = 10) Linewidth Versus Pressure.

the pure collisional widths by deconvolving the Doppler and laser lineshape from the total lineshape. This deconvolution is omitted from the present analysis because the error will be small for the higher pressure data points where pressure broadening dominates. In all three cases the data is reasonably linear in spite of the fact that the pressure broadened linewidth only contributes about one third of the total linewidth at the lowest pressures (50 torr). The uncertainty in reading the total linewidth for each data point was ± 40 MHz, indicated by a sample error bar in each figure. The uncertainty in reading the pressure is equal to the width of the data points. Pressure broadening coefficients were determined from linear least square fits to the data. In all cases, the y-intercept (pressure = 0 torr) linewidth corresponds to the approximate sum of the calculated Doppler (160 MHz) and measured laser (100 MHz) linewidths.

The present measurements are compared with the results of reference 35 in Table 5.5 and the agreement is generally good. Uncertainties for the present results that are listed in Table 5.5 correspond to one standard deviation of the slope from the linear fits. Most likely, there are systematic errors in the low pressure data points of the present results that are due to the laser and Doppler contributions to the linewidths. These systematic errors may account for the small offset in the two sets of results listed in Table 5.5.

Table 5.5

Pressure Broadening Coefficients [cm^{-1} (FWHM)/atm] for the v = 0 → 1 Q-Branch in N_2

	Present Work		Ref. 35
Q (J)	Intercept (MHz)	slope cm^{-1}/atm.	cm^{-1}/atm
6			.092 (4)
7			.090 (8)
8	290	.082 (6)	.090 (4)
9	290	.077 (2)	.088 (8)
10	294	.082 (2)	.086 (6)
11			.082 (10)
12			.080 (4)

CHAPTER 6

Conclusions

A non-intrusive and direct measurement of supersonic N_2 flow velocities has been demonstrated, in a laboratory environment, using inverse Raman spectroscopy (IRS). The velocities measured were of the order of 500 m/s with statistical uncertainties of 15 m/s. Higher velocities would pose no additional problems and, since the absolute errors of 15 m/s would remain fixed, the percentage uncertainties would be reduced. For the same reason, small velocities (< 100 m/s) would have larger percentage errors and could not be accurately measured with this Raman technique. Since the signal-to-noise ratio of the Raman spectra used for velocity measurements was 10 times greater than the shot noise limit and was dominated by some combination of laser fluctuations, there is room for improvement. A division scheme (not employed in the present work) should help improve the accuracy of this technique. The long term stability of the cw probe laser and the 100 MHz bandwidth of the pulsed pump laser are also limitations in these velocity measurements. One potential improvement is to lock the cw probe laser to an I_2 hyperfine transition rather than to the Doppler broadened transition as in this work. The bandwidth of the pulsed pump laser is another limitation in these measurements. Reduction of the pump laser bandwidth to 30 MHz or less would make the Raman

spectral profile (350 MHz at 50 torr) independent of the pump laser lineshape. Thus translational temperature and pressure could be determined by fitting Voigt profiles to the experimental lineshapes.

Non-intrusive rotational temperature and number density measurements have also been made in the supersonic flow. Temperature precisions were about 4 K for measurements at 150 K, while at 300 K they were about 8 K. Density measurements at temperatures of 150 K had uncertainties of 11% of the measured density. Although the velocity, temperature, and density measurements in this work were not made simultaneously, there is no fundamental reason why this could not have been done. Thus this work demonstrates the feasibility of simultaneous velocity, temperature, and density measurements of a supersonic flow using coherent Raman spectroscopy. Recently, measurements similar to those made here have been demonstrated in the Unitary Plan supersonic wind tunnel at NASA - Langley Research Center[45] by Dr. R. Exton's group, with whom we have been cooperating.

Although this work represents a significant step towards the goal of noninvasive, instantaneous, multiple point, supersonic flow parameter measurements, improvements beyond the present results are necessary before this goal can be achieved. First, the spatial resolution of the present measurement (1 cm) is too large for some of the smaller wind tunnels. Crossing the two laser beams would allow both higher spatial resolution and simultaneous multicomponent velocity measurements. Coherent Raman velocity measurements in two perpendicular directions with 1 mm spatial resolution have recently been reported[46] by our research group.

A drawback to coherent Raman velocity measurements made to date is the long (10 min) averaging times necessary to achieve accuracies less than 10%. The capability of obtaining accurate measurements with small ($\leq$ 1 sec) integration times would greatly enhance the usefulness of the Raman method. Thus one area of future research that would be of value is the reduction of measurement times. One method has already been proposed[47] and is similar to methods used for very short time (10 ns) temperature measurements.[48,49] The experimental demonstration of complete velocity measurements in a single 10 ns laser pulse would provide the opportunity for the study of turbulent phenomena on the nanosecond timescale. A second area for future investigation is the demonstration of simultaneous multipoint measurements. The present work was limited to measuring velocities at a single point. A demonstrated capability of measuring velocities at hundreds of different spatial points simultaneously would also increase the value of this Raman technique.

Based on the results of this thesis, one can predict that the coherent Raman technique has the potential of simultaneously measuring the velocities at 10^2 different points in a single 10 nsec laser pulse with the same precision as reported in the present work. The present measurements were made by averaging the IRS signal over 10^3 laser pulses, using a 1 MW pump laser and a 0.01 W probe laser. In Chapter 5, however, it was shown that a Coherent Raman Stokes Spectroscopy (CSRS) would be expected to have the same signal-to-noise ratio as an IRS measurement. Consider a CSRS velocity measurement which uses a 1 MW peak power pump laser, and a 10 MW broadband probe laser. The broadband probe laser will generate

CSRS signal over the complete Raman spectral profile in a single pulse. Since the CSRS signal is proportional to the probe laser power, there will be 10^9 more signal photons per laser pulse than in the present CSRS work. If the velocity measurement is restricted to a single pulse, there are still 10^6 more signal photons available than in the present CSRS measurement. If both the laser powers are divided equally among the 10^2 spatial points, the CSRS signal for a single point is 10^6 times smaller than if the laser powers remain undivided (since CSRS signal $\propto P_{pump}^2 \times P_{probe}$). Thus the total number of signal photons available from a single spatial point is comparable to the present measurements, and the proposal of 10^2 simultaneous velocity measurements in a single 10 nsec laser pulse seems possible, at least in principle. The technical details of such a measurement will prove to be difficult, but the potential benefits of such a measurement provide reason enough to consider an experimental demonstration. The achievement of this goal would furnish the aerodynamicist with a powerful tool for investigating supersonic gas flows.

In addition to flow parameter measurements, the results of pressure broadening and absolute signal strength broadening results (at room temperature) show that the J dependence of the pressure broadening coefficient is small enough to be neglected for the accuracy ($\pm$ 5%) of the temperature measurements reported here. Thus rotational temperatures can be determined from relative peak height measurements rather than relative integrated area measurements of adjacent rotational lines. Finally, the measured absolute signal strengths for IRS and CSRS are in general agreement (typically a

factor of 3 difference) with the results of the classical theory of stimulated Raman scattering. This agreement shows that the classical theory and measured spontaneous Raman cross sections are sufficient for predicting expected signal strengths for applications of coherent Raman scattering.

REFERENCES

1. Y. Yeh and H. Z. Cummins, "Localized Fluid Flow Measurements with a He Ne Laser Spectrometer," Appl. Phys. Lett. 4, 176 (1964).
2. R. M. Huffaker, "Laser Doppler Detection Systems for Gas Velocity Measurements," Appl. Opt. 9, 1026 (1970).
3. G. C. Herring, S. A. Lee and C. Y. She, "Measurements of a Supersonic Velocity in a Nitrogen Flow Using Inverse Raman Spectroscopy," Opt. Lett. 8, 214 (1984).
4. G. C. Herring, W. M. Fairbank, Jr., and C. Y. She, "Observation and Measurement of Molecular Flow Using Stimulated Raman Gain Spectroscopy," IEEE J. Quantum. electron., QE-17, 1975 (1981).
5. E. K. Gustafson, J. C. McDaniel and R. L. Byer, "CARS Measurement of Velocity in a Supersonic Jet," IEEE J. Quantrum Electron, QE-17, 2258 (1981).
6. C. Y. She, "Proposal for Measuring Molecular Velocity Vector with Single-Pulse Coherent Raman Spectroscopy," Appl. Phys. B, 32, 49-52 (1983).
7. W. Zapka and A. C. Tam, "Noncontact Optoacoustic Determination of Gas Flow Velocity and Temperature Simultaneously," Appl. Phys. Lett., 40, 1015 (1982).

8. Hiller, J. C. McDaniel, E. C. Rea, Jr., and R. Hanson, "Laser-Induced Fluorescence Technique for Velocity Field Measurements in Subsonic Flows," Opt. Lett. 8, 474 (1983).

9. J. V. Prodan, C. Y. She, W. M. Fairbank, Jr., "An Atomic Fluorescence Transit-Time Velocimeter," Opt. Comm. 43, 215 (1982).

10. M. Zimmerman and R. B. Miles, "Hypersonic-Helium-Flow-Field Measurements with the Resonant Doppler Velocimeter," Appl. Phys. Lett. 37, 885 (1980).

11. G. C. Herring, H. Moosmuller, S. A. Lee, and C. Y. She, "Flow Velocity Measurements with Stimulated Rayleigh-Brillouin-Gain Spectroscopy," Opt. Lett. 8, 602 (1983).

12. Bloembergen, Nonlinear Optics, Benjamin/Cummings, Reading, Massachusetts, Chapter 1 (1977).

13. A. Yariv, Introduction to Optical Electronics, Holt Rinehart and Winston, New York, page 207 (1976).

14. J. D. Jackson, Classical Electrodynamics, Wiley, New York, page 396 (1975).

15. A. Yariv, Introduction to Optical Electronics, Holt Rinehart and Winston, New York, page 208 (1976).

16. A. Yarvi, Quantum Electronics, Wiley, New York pp. 420 (1975).

17. I. J. Bigio, R. S. Finn, J. F. Ward, Appl. Opt. Lett. 14, 336 (1975).

18. A. Yariv, Introduction to Optical Electronics, Holt Rinehart and Winston, New York, page 33.

19. Adelbert Owyoung, "Coherent Raman Gain Spectroscopy Using cw Laser Sources," IEEE J. Quantum Electron. QE-14, 192 (1978).

20. G. Herzberg, Molecular Spectra and Molecular Structure I. Spectra of Diatomic Molecules, Van Nostyand, New York, Chapter 3 (1950).

21. J. J. Sakurai, Advanced Quantum Mechanics, Addison-Wesley, Reading, Massachusetts, Chapter 2 (1967).

22. G. Herzberg, Molecualr Spectra and Molecular Structure I. Spectra of Diatomic Molecules, Van Nostyand, New York, Chapter 3 (1950).

23. M. Zucrow and J. D. Hoffman, Gas Dynamics, John Wiley & Sons, New York (1976).

24. A. H. Shapiro, The Dynamics and Thermodynamics of Compressible Fluid Flow, Vol. I & II, Ronald Press Co., New York (1954).

25. V. L. Streeter, editor, Handbook of Fluid Dynamics, McGraw-Hill, New York (1961).

26. James E. John, Gas Dynamics, Allyan and Bacon, Boston (1969).

27. Same as Reference 4.

28. P. Drell and S. Chu, "A Megawatt Dye Laser Oscillator - Amplifier System for High Resolution Spectroscopy," Opt. Commun., 28, 343 (1979).

29. F. V. Kowalski, R. T. Hawkins and A. L. Schawlow, "Digital Wavemeter for CW Lasers," J. Opt. Soc. Am. 66, 965 (1976).

30. L. Hlousek and W. M. Fairbank, Jr., "High-Accuracy Wave-Number Measurements in Molecular Iodine," Opt. Lett. 8, 322 (1983).

31. T. W. Hansch, M. D. Levenson, and A. L. Schawlow, "Complete Hyperfine Structure of a Molecular Iodine Line," Phys. Rev. Lett. 26, 946 (1971).

32. A. Owyoung, "Inverse Raman Spectroscopy," in Laser Spectroscopy IV, Ed. H. Walther and K. W. Rothe, Springer Verlag, New York, 1979, p. 175.

33. Louis Hlousek (private communication).

34. W. M. Huo, "Optical Stark Effect in the Ro-Vibrational Spectrum of A Diatomic Molecule in the $^1\Sigma^+$ State and Numerical Calculations on N_2," NASA Ames Research Center, MS 230-3, Moffet Field, CA 94035 (unpublished).

35. G. J. Rosasco, W. Lempert, W. S. Hurst, and A. Fein, "Line Interference Effects in the Vibrational Q-Branch Spectra of N_2 and CO," Chem. Phys. Let. 97, 435 (1983).

36. C. E. Wieman, "Polarization Spectroscopy and the Measurement of the Lamb Shift in the Ground State of Hydrogen," Thesis: G. L. Report No. 2707, Stanford University.

37. Q. H. Lao, P. E. Schoen, and B. Chu, "Rayleigh-Brillouin Scattering of Gases with Internal Relaxation," J. Chem. Phys. 64, 3347 (1976).

38. Same as Reference 35.

39. Same as Reference 34.

40. H. U. Eckert, "Characteristics of the Turbulent Boundary Layer on a Flat Plate in Compressible Flow from Measurements of Friction in Pipes," Jour. Aero. Sci. 17, 573, (1950).

41. J. H. Keenan and E. P. Neumann, "Measurements of Friction in a Pipe for Subsonic and Supersonic Flow of Air," J. Appl. Mech., June, A-91, (1946).

42. J. Kaye, T. Y. Toong, and R. H. Shoulberg, "Measurement of Recovery Factors and Friction Coefficients for Supersonic Flow

of Air in a Tube," J. Appl. Mech., June, 185, (1952).

43. Same as Reference 24.

44. H. W. Schrötter and H. W. Klöckner, "Raman Scattering Cross Sections in Gases and Liquids," in Raman Spectroscopy of Gases and Liquids, edited by A. Weber (Springer, Berlin, 1979).

45. R. J. Exton and M. E. Hillard, "Raman Doppler Velocimetry: a Unified Approach for Measuring Molecular Flow Velocity, Temperature, and Pressure," Appl. Opt. 25, 14 (1986).

46. H. Moosmüller, G. C. Herring, and C. Y. She, "Two Component Velocity Measurements in a Supersonic Nitrogen Jet with Spatially Resolved Inverse Raman Spectroscopy," Opt. Lett. 9, 536 (1984).

47. Same as Reference 6.

48. Judith B. Snow, Jia-biao Zheng, and Richard Chang, "Spatially and Spectrally Resolved Multipoint Coherent Anti-Stokes Raman Scattering from N_2 and O_2 Flows," Opt. Lett. 8, 599 (1983).

49. Alan C. Eckbreth, Gregory M. Dobbs, John H. Stufflebeam, and Peter A. Tellex, "CARS Temperature and Species Measurement in Augmented Jet Engine Exhausts," Appl. Opt. 23, 1328 (1984).